

Response to Referee #1

General Comments: This is a very interesting study to investigate the impacts of agriculture fire emissions on temperature, precipitation, and clouds over East China. The study selected a typical event around June 10 2012 and conducted model simulations using WRF-Chem to examine the impacts. The results show that the absorbing aerosols emitted from the agriculture fire interacted with radiation and changed the meteorological conditions. This redistributes the precipitation over the downwind areas of the burning plumes. The results are well presented, and the topic is suitable for publication in ACP after addressing some specific comments listed below.

Response: We would like to thank the referee for providing the insightful suggestions, which indeed help us further improve the manuscript.

Specific Comments: 1. Since this study investigated the impacts of fire emissions on meteorological fields, more discussion about the fire emission inventory may be needed. In Section 2.1, please state what's the spatial and temporal resolution of the fire emission inventory used in this study. Section 3.4 discussed about the uncertainties that are partly from the fire emission spatial and vertical distributions. Did you compare your emission inventory with the FINN fire emission data (Wiedinmyer et al., 2011) that are with hourly temporal and 1x1 km² horizontal resolutions? In terms of vertical distribution of fire emissions, did you use the plume rise scheme in WRF-Chem or prescribe distribution profile? Please clarify.

Wiedinmyer, C., Akagi, S. K., Yokelson, R. J., Emmons, L. K., Al-Saadi, J. A., Orlando, J. J., and Soja, A. J.: The Fire INventory from NCAR (FINN): a high resolution global model to estimate the emissions from open burning, Geosci. Model Dev., 4, 625-641, doi:10.5194/gmd-4-625-2011, 2011.

Response: More descriptions on the fire emission inventory has been added in Section 2.1 in the revised manuscript. We compared the spatial patterns of FINN fire emission data (version 1.5) with the emission inventory used in this work. As shown in Fig. R1, they generally consistent with each other due to the fact that the location for the fires in both inventories are based on MODIS Thermal Anomalies Product. Some inconsistencies like the density of fire in central Jiangsu are attributed to the different land cover dataset applied for identification of underlying biomass type. FINN used MODIS Collection 5 Land Cover Type data while we employed Global Land Cover data. In terms of the spatiotemporal resolution, both the inventories were allocated to daily emissions for each 1 × 1 km grid. Technically, time information in FINN dataset shows time of satellite overpass/observation, not the duration of fire. Our inventory differs from FINN in magnitude.

Taking CO emission during the first half of June for the inner model domain, we estimate that 4.5 Tg CO was emitted while FINN gives the value of 7.5 Tg. That is caused by various methods to estimate burned biomass. FINN used MODIS Vegetation Continuous Fields to assign the burned mass. All farmland regardless what kinds of crop are cultivated was assumed to have a fuel loading of 0.5 kg/m². However, in China, crop straw is used in multiple ways, like biofuel, biogas production and animal feed supply, which is highly dependent on crop species. We estimated the emission using a “bottom-up” method by fully considering crop straw production, crop-specific usage and combustion efficiency. The smaller estimation was expectable.

We did not use the plume rise scheme for this biomass burning case, during which the burned biomass is winter wheat straw. Post-harvest crop residue is burned by flaming in mechanized agricultural systems. In contrast, when crops are harvested by hand the residue is often burned in piles that may smolder in China. It is noteworthy that the plume rise scheme is more suitable for the flaming phase (Freitas et al., 2007; Grell et al., 2011). In East China, especially in the northern Jiangsu and Anhui province, most fires of wheat straw are characterized by short-lived, small-scale smoldering (Fig. R2). Correspondingly, the fire radiative power (FRP) between this straw burning is much weaker than the grassland fire in North America (Fig. R3), indicating two different burning conditions. Thus in this work, the straw fire emission was placed in the lowest two levels from the surface to around 50 meter. We clarified these issues and mention the comparisons of FINN data and emission calculation in the revised Section 2.2.

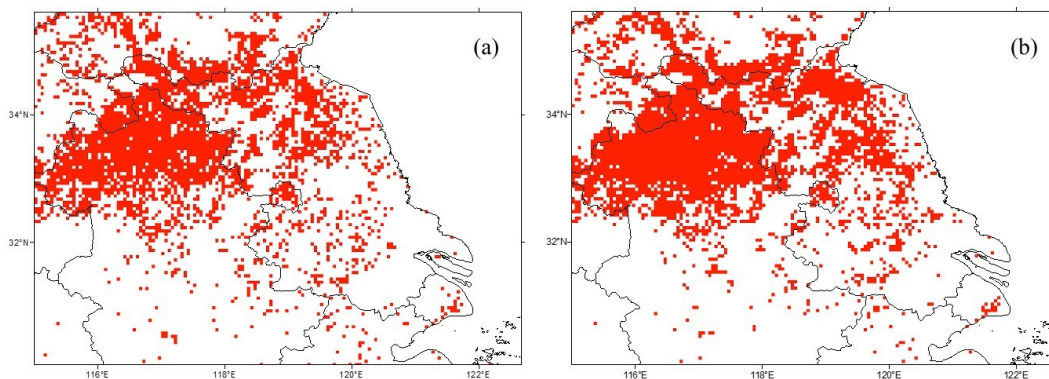


Fig. R1. Comparison of CO emission from biomass burning between FINN V1.5 emission and the emission inventory used in this study during the first half of June 2012. Here, FINN V1.5 dataset was acquired at <http://bai.acom.ucar.edu/Data/fire/>.



Fig. R2 A photo showing the field burning of wheat straw in Suixi county ($33^{\circ}54'37''\text{N}$, $116^{\circ}45'46''\text{E}$), northern Anhui province on June 14, 2013.

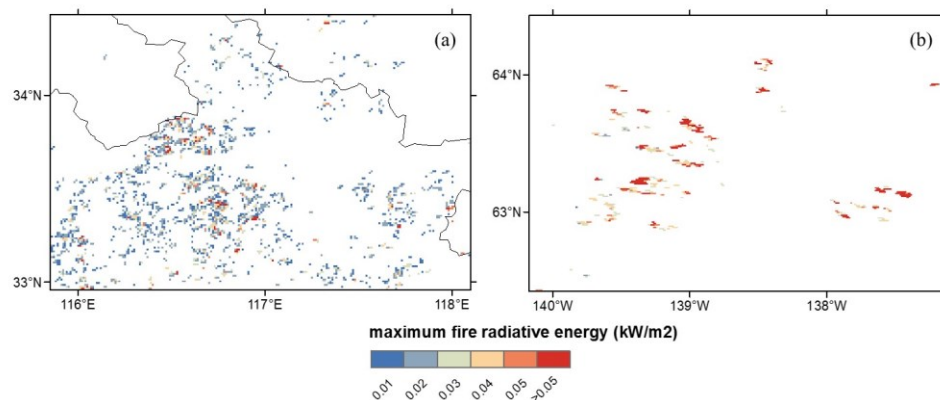


Fig. R3 MODIS-detect maximum fire radiative power (FRP) during crop straw fire in northern Anhui on 9 June 2012 and grassland fire in North America on 3 July 2004.

2. In Section 2.2, the simulation was conducted from May 20 to June 15, but the analysis as only for June 9-11. This is confused. I would suggest just mentioning that you have a simulation period for spin-up the chemistry initial condition. More importantly, please state what's the meteorological initializing date for the event of June 9-11. The different initializing date may change the results of impacts. Did you try different initializing date to see whether the results changed?

Response: Thanks for the suggestions. The meteorological initializing date was 12:00 UTC on 9 June. We have added the relevant descriptions in Section 2.2. We tried different initializing date, there are some discrepancies. Considering higher model performance of first 72-hour forecast and 12-hour spin-up, we think that it is practicable to set 12:00 UTC on 9 June as the initializing date for the simulation of 10 June when distinct precipitation modifications occurred.

3. In line 175 of page 6, I am not convinced that the ACI should be disabled for investigating ARI effect. Please explain why ACI should be disabled in this study? I think it will be more interesting to compare both ACI and ARI. Although authors pointed that previous studies found ARI sometimes is more important, this is not always the case (e.g., Zhong et al., 2015). Another critical issue of turning off ACI in WRF-Chem is about aerosol wet removal. In WRF-Chem, aerosol wet removal is linked with ACI. With turning off ACI, please clarify how you treat the wet removal of aerosols in your simulations since your event (Fig. 8) shows significant amounts of precipitation.

Zhong, S., Y. Qian, C. Zhao, R. Leung, and X.-Q. Yang (2015), A case study of urbanization impact on summer precipitation in the Greater Beijing Metropolitan Area: Urban heat island versus aerosol effects, *J. Geophys. Res. Atmos.*, 120, 903–10,914, doi:10.1002/2015JD023753.

Response: This work intended to investigate the effects of aerosol-radiation interaction, as pointed out in the title. Indeed, in some cases, ACI is of great importance, like in Zhong et al. (2015). However, previous studies and review papers indicated that under highly polluted conditions or strongly absorbing aerosol environment, ARI could be the dominant factor (Fan et al., 2008; Rosenfeld et al., 2008; Fan et al., 2015). Sensitivity simulations using cloud parcel model also suggest that CCN activation shows a weaker dependence on aerosol with increasing aerosol loadings, which is converting from an aerosol-limited regime to an updraft-limited regime (Reutter et al., 2009; Chang et al., 2015). We checked the relative sensitivity ratio proposed by Reutter et al. (2009) in Fig. R4. Relative sensitivity ratio less than $0.1 \times 10^{-3} \text{ m s}^{-1} \text{ cm}^3$ indicates that CCN activation and cloud drop formation was insensitive to the aerosol concentration during this case.

To further investigate the relative importance of ACI, we conducted another numerical experiment considering both ARI and ACI. Radiative perturbations caused by ARI far outweigh those from ACI at the TOA and at the ground surface, so did the adjustment in vertical temperature profile (Fig. R5-6). ACI could be a crucial factor modifying precipitation to large extent under some conditions (Zhong et al., 2015). In Zhong's case, the aerosol loading was much lower. As reported by the ministry of environmental protection of China, PM₁₀ concentrations were 126, 62 and 90 $\mu\text{g}/\text{m}^3$ in Beijing, Tianjin and Shijiazhuang on 28 June 2008. Furthermore, sulfate and other hygroscopic components dominate PM concentration during summer time in Beijing (Zhang et al., 2013), which might enhance aerosols' activity acting as CCN. Besides, stronger updraft motion may further favor aerosol-cloud interaction during the case in Zhong et al. (2015). By contrast, tremendous freshly-emitted hydrophobic carbonaceous aerosol from biomass burning together with weaker updraft motion may lead to less important role of ACI in this work.

Yes, in WRF-Chem, aerosol wet removal is disabled too if ACI is switched off. In our study, we mainly focused on the initialization of precipitation. As mentioned in the article, the modifications of precipitation onset mainly linked to the vertical re-allocation of short-wave energy due to absorbing aerosol during daytime, which was less affected by wet scavenging later that night. Therefore, ignoring wet scavenging is acceptable here. However, considering the referee's points, we added a few sentences to address the uncertainty of our treatment in Section 2.2.

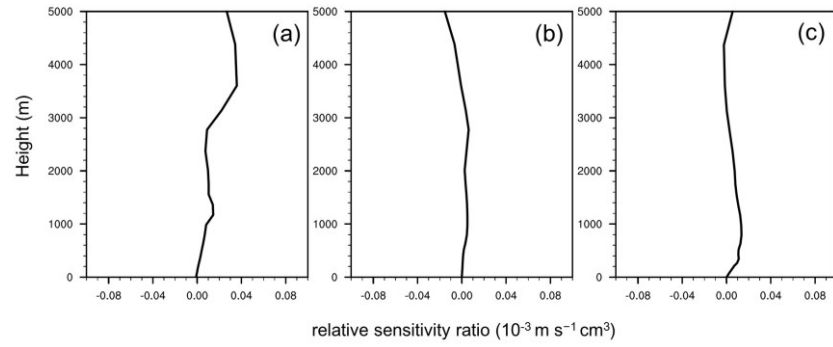


Fig. R4. Vertical profile of relative sensitivity ratio proposed by Reutter et al., (2009) during the precipitation for three region marked in Fig.8: Zone 1(a), Zone 2 (b), and Zone 3 (c).

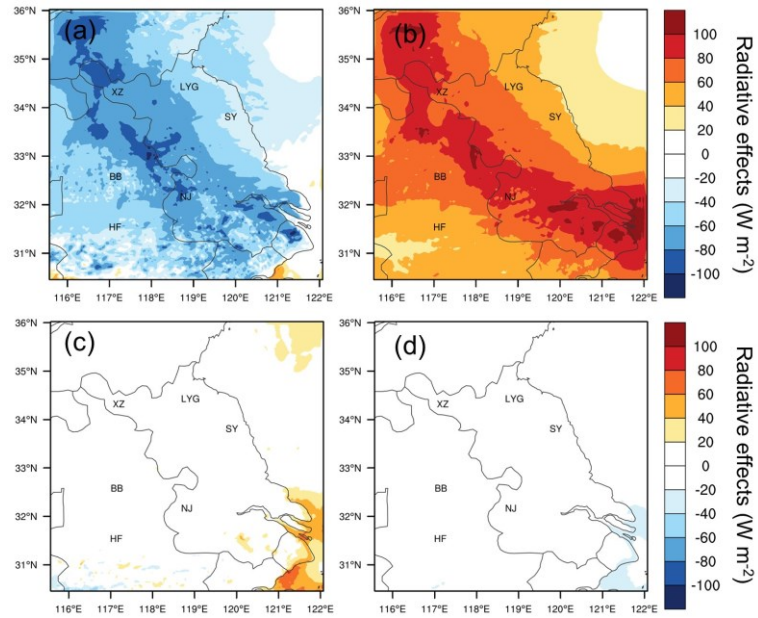


Fig. R5. Radiative forcing of ARI at the surface (a) and in the atmosphere (b) on 10 June. Radiative forcing of ACI at the surface (c) and in the atmosphere (d) on 10 June.

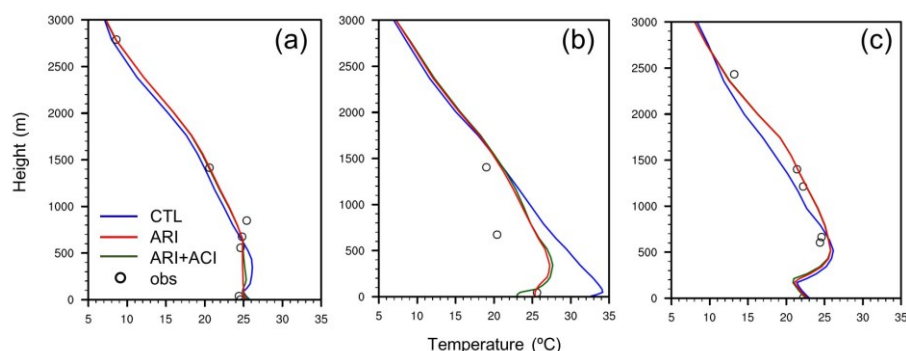


Fig. R6. Comparisons between the observed and modelled air temperature profiles for (a) NJ (Nanjing) at 08:00 LT, (b) XZ (Xuzhou) and (c) SY (Sheyang) at 20:00 LT, 10 June. Black circles denote sounding observations. Blue, red and green solid lines are numerical experiments without (CTL), with radiative effects of aerosols (ARI), and with both ARI and ACI (aerosol-cloud interaction), respectively.

4. This study highlighted the impacts of fire emissions, however, the experiments were only designed with CTL and ARI. Based on these two experiments, it's hard to disentangle the biomass burning effect from the effects of anthropogenic aerosols. One experiment without biomass burning emissions is needed if the purpose is to investigate the impacts of agriculture fire.

Response: Accepted. Another experiment without biomass burning emissions have been conducted and discussed further in the revised manuscript.

5. In lines 219-221 of page 8, please provide the corresponding simulated values as well.

Response: Accepted. The corresponding simulated values have been provided.

6. In Fig. 3, do you have hourly observations? If not, why not also put daily mean of simulated values for a direct comparison?

Response: Accepted. We re-plotted Figure 3 using daily mean of simulated PM₁₀ concentrations.

7. In Fig. 4, why not show the simulated SSA?

Response: In the further analysis in section 3.3, BC played a vital role in precipitation modification. Showing its spatial pattern provides a more direct and clear picture of how BC was transported and distributed than that of SSA.

8. Section 3.3, Fig. 8, it seems to me that model has large biases in capturing spatial distributions of TRMM precipitation. Can you try another precipitation dataset (CMORPH) for comparison? CMORPH provides 8 km resolution data. Is this poor comparison between model and TRMM due to the initial condition? Did you try different initial meteorological conditions? In addition, this may be also partly due to the missing of aerosol-cloud interaction? Strong suggestion to test this case with aerosol cloud interaction.

Response: Fig. R7 shows the comparison of spatial distributions between CMORPH and TRMM satellite-based precipitation on 10 June 2012. As shown, there is no significant difference in spatial patterns. Specifically, no precipitation in Nanjing and the surrounding areas, and precipitation exceeding over 10 mm took place in northern Jiangsu. Indeed, the simulation did not compare well with the satellite observations. We have also tried ECWMF ERA Interim data to initiate the regional model, which cannot well describe the pattern either. As mentioned above, including ACI exert little effect on the radiation flux and temperature stratification. Actually, we have tried a series of simulations with different initial meteorological conditions and various parameterization schemes. Almost all the setups failed to represent such high aerosol loadings (Fig. 3). It is suggested that rapid formation of secondary aerosol, like sulfate and SOA, might be significantly underestimated due to a limited understanding of SOA formation and its optical properties and also heterogeneous chemistry that enhanced the oxidizing capacity of the atmosphere during this biomass-burning case (Xie et al., 2015). Our group will keep working on the secondary transformations of aerosol and the radiative effects during agricultural fires with more in-site measurements.

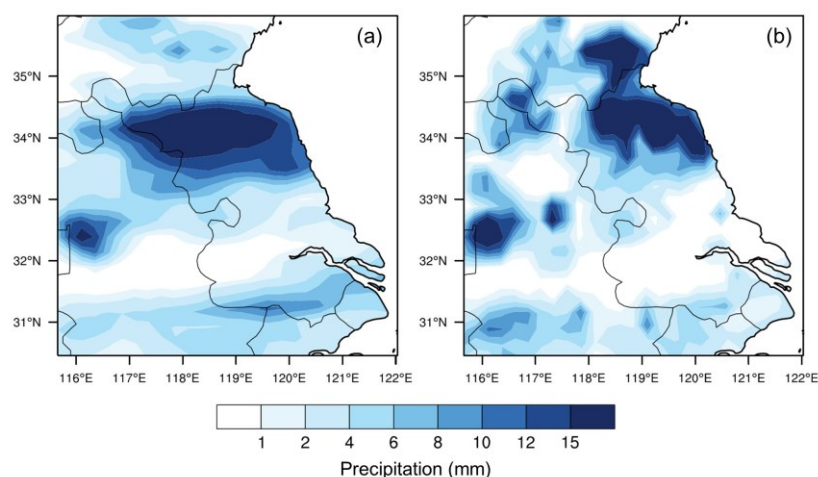


Fig. R7 (a) Spatial distributions of CMORPH satellite-based daily precipitation on 10 June 2012 (b) Corresponding TRMM-observed precipitation. The CMOPRH data was obtained from <http://rda.ucar.edu/datasets/ds502.0/>.

9. *I don't see the necessity to include the paragraph of Line 331-337 of page 12.*

Response: Accepted. This paragraph has been removed in the revised version.

References

- Chang, D., Cheng, Y., Reutter, P., Trentmann, J., Burrows, S., Spichtinger, P., Nordmann, S., Andreae, M., Pöschl, U., and Su, H.: Comprehensive mapping and characteristic regimes of aerosol effects on the formation and evolution of pyro-convective clouds, *Atmos Chem Phys*, 15, 10325-10348, 2015.
- Fan, J. W., Zhang, R. Y., Tao, W. K., and Mohr, K. I.: Effects of aerosol optical properties on deep convective clouds and radiative forcing, *J Geophys Res-Atmos*, 113, ArtD08209, 10.1029/2007jd009257, 2008.
- Fan, J. W., Rosenfeld, D., Yang, Y., Zhao, C., Leung, L. R., and Li, Z. Q.: Substantial contribution of anthropogenic air pollution to catastrophic floods in Southwest China, *Geophys Res Lett*, 42, 6066-6075, 10.1002/2015GL064479, 2015.
- Freitas, S. R., Longo, K. M., Chatfield, R., Latham, D., Silva Dias, M., Andreae, M., Prins, E., Santos, J., Gielow, R., and Carvalho Jr, J.: Including the sub-grid scale plume rise of vegetation fires in low resolution atmospheric transport models, *Atmos Chem Phys*, 7, 3385-3398, 2007.
- Grell, G., Freitas, S. R., Stuefer, M., and Fast, J.: Inclusion of biomass burning in WRF-Chem: impact of wildfires on weather forecasts, *Atmos Chem Phys*, 11, 5289-5303, DOI 10.5194/acp-11-5289-2011, 2011.
- Reutter, P., Su, H., Trentmann, J., Simmel, M., Rose, D., Gunthe, S., Wernli, H., Andreae, M., and Pöschl, U.: Aerosol-and updraft-limited regimes of cloud droplet formation: influence of particle number, size and hygroscopicity on the activation of cloud condensation nuclei (CCN), *Atmos Chem Phys*, 9, 7067-7080, 2009.
- Rosenfeld, D., Lohmann, U., Raga, G. B., O'Dowd, C. D., Kulmala, M., Fuzzi, S., Reissell, A., and Andreae, M. O.: Flood or drought: How do aerosols affect precipitation?, *Science*, 321, 1309-1313, 10.1126/science.1160606, 2008.
- Xie, Y. N., Ding, A. J., Nie, W., Mao, H. T., Qi, X. M., Huang, X., Xu, Z., Kerminen, V. M., Petaja, T., Chi, X. G., Virkkula, A., Boy, M., Xue, L. K., Guo, J., Sun, J. N., Yang, X. Q., Kulmala, M., and Fu, C. B.: Enhanced sulfate formation by nitrogen dioxide: Implications from in situ observations at the SORPES station, *J Geophys Res-Atmos*, 120, 12679-12694, 10.1002/2015JD023607, 2015.
- Zhang, R., Jing, J., Tao, J., Hsu, S.-C., Wang, G., Cao, J., Lee, C. S. L., Zhu, L., Chen, Z., Zhao, Y., and Shen, Z.: Chemical characterization and source apportionment of PM_{2.5} in Beijing: seasonal perspective, *Atmos. Chem. Phys.*, 13, 7053-7074, doi:10.5194/acp-13-7053-2013, 2013.
- Zhong, S., Qian, Y., Zhao, C., Leung, R., and Yang, X. Q.: A case study of urbanization impact on summer precipitation in the Greater Beijing Metropolitan Area: Urban heat island versus aerosol effects, *Journal of Geophysical Research: Atmospheres*, 120, 2015.

Response to Referee #2

The authors provides an interesting and instructive work on the radiation effect of aerosols from biomass burning and the impacts on meteorological parameters including clouds, temperature, relative humidity, and rainfall in East China by conducting two parallel numerical simulations with the online coupled model WRF-Chem. The experiments are well designed and the presented results are generally convinced. Overall, I believe that it is a valuable study to highlight the importance of straw burning in weather modifications as well as air quality deterioration. It is worth to be published in ACP after adding more in-depth discussion of the simulated results. The specific comments are shown as follows.

Response: We would like to appreciate the referee for providing such great suggestions. We have conducted more simulations and revised this article according to the suggestions.

As pointed out in the present work, BC was the most important factor that alters the radiation budget. However, in the ARI simulation, BC was emitted not only from crop straw burning, but also from residential combustion and transportation, especially in anthropogenic emission-intensive region like East China. It is hard to figure out the effects of straw burning through these two simulations. Thus, this work would be further improved by isolating the radiative forcing just caused by straw fires during this biomass burning case. Quantitative comparisons between radiative effects induced by agricultural fires and anthropogenic pollutants could make more sense.

Response: Accepted. Another experiment without biomass burning emissions has been conducted and discussed in detail in the revised manuscript.

Some of the detailed descriptions on the method part need to be clarified, for instance, how the estimated emissions were allocated using MODIS detections. It should be noted that detected fire spots could be caused by forest or grassland fires, rather than crop straw burning.

Response: Accepted. We have added more detailed descriptions on the method of development of emission inventory and how the crop straw burning was identified. Please see Section 2.1.

Another deficiency of this paper is that while discussing the precipitation redistribution in Section 3.3, there is a lack of an in-depth analysis of how or through which processes the fire plumes influence the temperature stratification and moisture conditions. It is can be further improved by adding some diagnoses like CAPE (convective available

potential energy) or MSE (moist static energy), which may provide more direct evidence (Fan et al., 2015).

Response: Accepted. MSE has been used a prognostic parameter in the discussion. Please see Figure 10-12 and Section 3.3.2.

In addition to the main concerns above, additional minor comments are given below.

Minor comments:

1) Line 173 and 174: Define ARI and CCN when they first appeared.

Response: Accepted. The definition of the abbreviation has been added.

2) Line 214: Change Air Pollution Index (API) to Air Quality Index (AQI)

Response: Before the year of 2013, the ministry of environmental protection of China reported API data instead of AQI. Since the study period of this work is 2012, the data we can acquire was API.

3) Caption of Fig.10: the unit of cloud water mixing ratio should be “g kg⁻¹”.

Response: Accepted. Please see the caption of Figure 10.

4) Line 360: the sentence “For the humidity perturbations” is better to be rephrased to “the perturbations in humidity”.

Response: Accepted.

**Effects of aerosol-radiation interaction on precipitation during
biomass-burning season in East China**

**Xin Huang^{1,2,3}, Aijun Ding^{1,2,3*}, Lixia Liu^{1,2}, Qiang Liu^{1,2}, Ke Ding^{1,2}, Wei Nie^{1,2,3}, Zheng
Xu^{1,2,3}, Xuguang Chi^{1,2,3}, Minghuai Wang^{1,2,3}, Jianning Sun^{1,2,3}, Weidong Guo^{1,2,3}, and
Congbin Fu^{1,2,3}**

¹Joint International Research Laboratory of Atmospheric and Earth System Sciences, Nanjing
University, China

²Institute for Climate and Global Change Research & School of Atmospheric Sciences, Nanjing
University, Nanjing, 210023, China

³Collaborative Innovation Center of Climate Change, Jiangsu Province, China

* Correspondence to: Aijun Ding (dingaj@nju.edu.cn)

Abstract

Biomass burning is a main source for primary carbonaceous particles in the atmosphere and acts as a crucial factor that alters Earth's energy budget and balance. It is also an important factor influencing air quality, regional climate and sustainability in the domain of Pan-Eurasian Experiment (PEEX). During the exceptionally intense agricultural fire season in mid-June 2012, accompanied with rapidly deteriorating air quality, a series of meteorological anomalies was observed, including a large decline in near-surface air temperature, spatial shifts and changes in precipitation in Jiangsu Province of East China. To explore the underlying processes that link air pollution to weather modification, we conducted a numerical study with parallel simulations using the fully coupled meteorology-chemistry model WRF-Chem with a high-resolution emission inventory for agricultural fires. Evaluation of the modelling results with available ground-based measurements and satellite retrievals showed that this model was able to reproduce the magnitude and spatial variations of fire-induced air pollution. During the biomass-burning event in mid-June 2012, intensive emission of absorbing aerosols trapped a considerable part of solar radiation in the atmosphere and reduced incident radiation reaching the surface on a regional scale, followed by lowered surface sensible and latent heat fluxes. The perturbed energy balance and re-allocation gave rise to substantial adjustments in vertical temperature stratification, namely surface cooling and upper-air heating. Furthermore, intimate link between temperature profile and small-scale processes like turbulent mixing and entrainment led to distinct changes in precipitation. On one hand, by stabilizing the atmosphere below and reducing the surface flux, black carbon-laden plumes tended to dissipate daytime cloud and suppress the convective precipitation over Nanjing. On the other hand, heating aloft increased upper-level convective activity and then favored convergence carrying in moist air, thereby enhancing the nocturnal precipitation in the downwind areas of the biomass burning plumes.

1 Introduction

Biomass burning, defined as open or quasi-open combustion of non-fossilized vegetative or organic fuel, is widely used by humans to manage and transform land cover for many purposes and has been identified as one of the most important disturbance agents in world's terrestrial ecosystems (Fearnside, 2000). It is a major source of many trace gases and particulate matters on a regional and a global scale (Andreae and Merlet, 2001; van der Werf et al., 2006; Ito et al.,

2007), contributing significantly to the budgets of trace gases, greenhouse gases and atmospheric aerosols (Langenfelds et al., 2002). For instance, biomass burning is estimated to be responsible for almost half of global carbon monoxide (CO) emission and more than one third of total black carbon (BC) emission (Bergamaschi et al., 2000; Bond et al., 2013). With tremendous and intensive emission of atmospheric pollutants, it has been recognized as one of the culprits of regional air pollution (Wiedinmyer et al., 2006; Ryu et al., 2007) and an important disturber of biogeochemical cycles, especially for those of carbon and nitrogen (Crutzen and Andreae, 1990; Kuhlbusch, 1998). In the Eurasian continent, i.e., the domain of Pan-Eurasian Experiment (PEEX) (Kulmala et al., 2015), biomass burning is a very important source influencing air quality, regional climate change and sustainability (Chi et al., 2013; Ding et al., 2013ab; Lappalainen et al., 2016). In the East China, the impact of biomass burning to air quality and regional climate change is particularly interesting because of the mixing of biomass burning plumes with pollutant from fossil fuel combustion sources (Ding et al., 2013a; Nie et al., 2015; Xie et al., 2015; Lappalainen et al., 2016).

Biomass burning, including forest fires, savanna fires, peat burning, and crop residue burning in field, generally features a high emission rate of light-absorbing carbonaceous aerosols (Reid et al., 1998; Schwarz et al., 2008). The most important one is BC, which is intensively emitted during biomass burning events due to incomplete combustions (Reid et al., 2005; Akagi et al., 2011). As the dominant absorber of solar radiation in the atmosphere, BC warms the Earth-atmospheric system and alters the partitioning of energy between the ground surface and the atmosphere, thereby modifying atmospheric thermodynamic structures and modulating hydrological cycles (Krishnan and Ramanathan, 2002; Ramanathan et al., 2005; Ding et al., 2016). These modifications induced by biomass burning have been detected in many regions, especially for those during forest fires. Surface temperature decline was extensively observed during forest fires in North America, Asia and Africa (Robock, 1988, 1991; Procopio et al., 2004; Kolusu et al., 2015). The dimming around ground surface and heating in the upper-atmosphere, especially in the upper boundary layer, could cause the suppression of daytime mixing height and result in an enhancement of surface air pollution through aerosol-boundary layer-radiation feedbacks (Ding et al., 2013a; Ding et al., 2016). This effect was named as the “Dome Effect” of BC by Ding et al. (2016). By cooling the surface and stabilizing the atmosphere, intense forest fire may lead to the inhibition of cloud formation (Andreae et al., 2004; Koren et al., 2004; Feingold et al., 2005), suppression in precipitation (Rosenfeld, 1999; Sakaeda et al., 2011), and even temporal shift in onset of monsoon (Liu et al., 2005; Lau et al.,

2006; Zhang et al., 2009). In one word, BC has been demonstrated to cause a significant perturbation in the radiative energy balance and has even led to regional and global climate change (Penner et al., 1992; Menon et al., 2002; Ramanathan and Carmichael, 2008).

Although forest and savanna fires are much less notable in China compared with tropical America, Africa and Southeast Asia (van der Werf et al., 2006), it is noteworthy that China is a large country with the world's top-ranked agricultural production, which is inevitably accompanied by a tremendous amount of crop residue. Field burning of crop residue is a common and wide-spread management practice in China during post-harvest periods for the purpose of clearing farmland and providing short-lived ash fertilization for the crop rotation (Gao et al., 2002). It is estimated that about 120 Tg crop residues were burned in field across China every year, far higher than those burned in forest fires and savanna fires (Yan et al., 2006). Previous studies have documented that field burning of crop residue led to deterioration in regional air quality during harvest season (Yang et al., 2008; Huang et al., 2012b; Li et al., 2014). What is worse, this kind of pollution occurs periodically in East China, particularly during the harvest period of wheat in June (Figure 1). However, studies regarding its effects on meteorology and climate are still limited. Ding et al. (2013a) reported that temperature and precipitation were dramatically modified during the harvest season in 2012 according to ground based measurements at a regional background station SORPES in the Yangtze River Delta region in East China (Ding et al., 2013b). However, there is a lack of a comprehensive picture of how or through which processes the biomass burning plumes influenced the air temperature and precipitation and on what scale the aerosol-weather interactions happened during this case.

Here we conducted numerical simulations for the biomass burning event in East China during mid-June 2012 based on the online coupled meteorology–chemistry model WRF-Chem (the Weather Research and Forecasting model coupled with Chemistry) combined with multiple ground-based measurements and remote-sensing retrievals. The rest of this paper is structured as follows: Section 2 describes the development of an emission inventory for field burning of crop residues and how the numerical simulations are configured and designed; in Section 3 we validate the modelling results using available measurements, and then analyse the perturbations in energy budget and temperature adjustments induced by crop residue burning; finally, three regions with distinct precipitation changes, located near or downwind from the burning sites, are selected to discuss in detail. Conclusions are drawn in Section 4.

2 Data and Methodology

2.1 Emission inventory

Modelling aerosols' radiative effects during this biomass burning event first requires accurate quantification and meticulous characterization of emission from field burning of crop residue. Here, emission intensities of trace gases and particulate matters, specifically including carbon dioxide (CO₂), CO, methane (CH₄), Non-Methane Organic Compounds (NMOCs), nitrogen oxides (NO_x), ammonia (NH₃), sulfur dioxide (SO₂), BC, organic carbon (OC), and particulate matter (PM_{2.5} and PM₁₀ are particles with aerodynamic diameter less than 2.5 and 10 microns, respectively), were estimated based on a bottom-up method. According to the farming season (available at zzys.agri.gov.cn) and province-level statistics on crop cultivation (NBSC, 2013), we can deduce that the intensive agricultural fires in June were mainly related to wheat straw burning as a consequence of the extensively spreading cultivation mode of "winter wheat-summer corn/rice" in East China. Burned biomass at province-level was calculated based on statistical data of crop productions, residue-to-production ratios, percentages of crop residues burned in the field. Emissions of various pollutants were derived from the product of burned mass and experiment results on crop-specific combustion efficiencies and pollutant-specific emission factors. The detailed methods and involved datasets are described in our previous work (Huang et al., 2012b).

To determine the locations and time of crop residue fires, MODIS (Moderate Resolution Imaging Spectroradiometer) Thermal Anomalies/Fire Daily L3 Global Product (MOD/MYD14A1) combined with burned area product (MCD45A1) were introduced for the purpose of emission spatiotemporal allocations (Giglio et al., 2003; Boschetti et al., 2009). MOD/MYD14A1 provides fire identification by examining the brightness temperature relative to neighbouring pixels. MCD45A1 was also incorporated in this work because its bidirectional reflectance model-based change detection approach has been proved to be capable of presenting a more accurate mapping of smaller fragments of burn scars (Roy and Boschetti, 2009). [Global Land Cover \(GLC\) product with a spatial resolution of 1 km was used in this study to identify the burning of different biomass. Only fire detections that occurred on farmland, that is land cover classes defined as "Farm" and "Mosaic of cropping", was identified as field burning of crop residue. Emission at province level estimated using the aforementioned method were then allocated equally to each fire spot.](#)

The fire emission estimation developed in this work was compared with the FINN fire emission dataset. Spatially, these two emission inventories generally were consistent with each other because the locations for the fires in both inventories are based on MODIS Thermal Anomalies Product (Figure S1). Some inconsistencies, such as the density of fire in central Jiangsu, are attributed to the different land cover dataset applied for the identification of underlying biomass type. FINN fire emission estimation used MODIS Collection 5 Land Cover Type data (Wiedinmyer et al., 2011), while we employed Global Land Cover data. This inventory differs slightly from FINN estimation in magnitude. Taking CO emission in the inner model domain for instance, we estimate that 4.5 Tg CO was emitted while FINN gives the value of 7.5 Tg during the first half of June 2012. It might be attributed to different methods to estimate burned biomass. FINN used MODIS Vegetation Continuous Fields to assign the burned mass. The fuel loading of farmland was assumed to be 0.5 kg/m² (Wiedinmyer et al., 2006). However, in China, crop straw is used in multiple ways that differ regionally, like biofuel, biogas production and animal feed supply, which is highly dependent on crop species. We estimated the emission using a “bottom-up” method by fully considering crop yields, crop-specific straw usage and combustion efficiency.

During this agricultural fire event, the spatial pattern of fire detections in Figure 2a indicates that open burning of straw mostly concentrated in northern parts of Anhui and Jiangsu province and got extremely severe on 9 and 13 June, as displayed in Figure 2b. Burning of crop residues dominated local emissions of atmospheric pollutants when compared with corresponding anthropogenic emissions. Taking BC for instance (Figure 2c and d), emission rate from field burning of crop residues far outweighed that from industry, power plant, residential activity and transportation combined (Li et al., 2015).

2.2 Numerical simulation

The numerical simulations in this study were conducted using WRF-Chem version 3.6.1, which is an online-coupled chemical transport model considering multiple physical and chemical processes, including emission and deposition of pollutants, advection and diffusion, gaseous and aqueous chemical transformation, aerosol chemistry and dynamics (Grell, G. et al., 2011). The model has been widely utilized to investigate aerosol-radiation-cloud interactions and aerosol-boundary layer feedback (Grell, G. et al., 2011; Zhao, C. et al., 2013; Fan et al., 2015; Huang et al., 2015; Ding et al., 2016; Gao et al., 2016). In the present work, we adopted two nested model domains centred at 115.0°E, 33.0°N (Figure 1a). The parent domain with a grid

1 resolution of 20 km covered the eastern China and its surrounding areas to get synoptic forcing.
2 The fine resolution of 4 km for the inner one allowed better characterization of small-scale
3 physical processes, especially those linked to convective motions, cloud formation and rainfall
4 onset. There were 31 vertical layers from the ground level to the top pressure of 50 hPa, 20 of
5 which were placed below 4 km to achieve finer vertical resolution within the boundary layer.
6 The initial and boundary conditions of meteorological fields were updated from the 6-hour
7 NCEP (National Centres for Environmental Prediction) global final analysis (FNL) data with a
8 $1^\circ \times 1^\circ$ spatial resolution. To investigate the aerosols' radiative effects on 10 June 2012 when
9 the precipitation was substantially modified, the simulations were conducted for the time period
10 from 20 May to 15 June. The meteorological initializing date for 10 June was 12:00 UTC on 9
11 June. Each run covered 60 hours and the last 48-hour modelling results were kept. The chemical
12 outputs from the preceding run were used as the initial conditions for the following run. The
13 first 20 days were regarded as the model spin-up period for atmospheric chemistry, so as to
14 better characterize aerosol distributions and minimize the influences of initial conditions and
15 allow the model to reach a state of statistical equilibrium under the applied forcing (Berge et
16 al., 2001; Lo et al., 2008).

17 Key parameterization options for the WRF-Chem modelling were the Noah land surface
18 scheme to describe the land-atmosphere interactions (Ek et al., 2003), the YSU boundary layer
19 scheme (Hong, 2010), and the RRTMG short- and long-wave radiation scheme (Mlawer et al.,
20 1997). The Lin microphysics scheme that accounts for six forms of hydrometeor (Lin et al., 1983)
21 together with the Grell cumulus parameterization was applied to reproduce the cloud and
22 precipitation processes (Grell, G. A. and Devenyi, 2002) for the coarse domain. Cumulus
23 parameterization was switched off for the inner domain. For the numerical representation of
24 atmospheric chemistry, we used the CBMZ (Carbon-Bond Mechanism version Z)
25 photochemical mechanism combined with MOSAIC (Model for Simulating Aerosol
26 Interactions and Chemistry) aerosol model (Zaveri and Peters, 1999; Zaveri et al., 2008).
27 Aerosols were assumed to be spherical particles. The size distribution was divided into four
28 discrete size bins defined by their lower and upper dry particle diameters (0.039–0.156, 0.156–
29 0.625, 0.625–2.5, and 2.5–10.0 μm). Aerosols in each size bin were assumed to be internally
30 mixed and their optical properties, including extinction coefficient, single-scattering albedo
31 (SSA) and asymmetry factor, were computed based on Mie theory (Fast et al., 2006) using
32 volume averaged refractive indices (Barnard et al., 2010). Similar model configurations and
33 settings have achieved good performance in our previous simulations over the eastern China

(Huang et al., 2015; Ding et al., 2016). Detailed configurations and domain settings are listed in Table 1.

Both natural and anthropogenic emissions were included for the regional WRF-Chem modelling in the present work. Typical anthropogenic emissions were obtained from the Multi-resolution Emission Inventory for China (MEIC) database (Li et al., 2015), in which emissions sources were classified into five main sectors: power plants, residential combustion, industrial processes, on-road mobile sources, and agricultural activities. This database covers most of anthropogenic pollutants, such as SO₂, NO_x, CO, volatile organic compounds (VOCs), PM, BC, and OC. NH₃ emission over China was derived from Huang et al. (2012a). VOCs emitted from typical anthropogenic activities and aforementioned crop residue burning were speciated into model-ready lumped species using profiles for Carbon-Bond Mechanism (Hsu et al., 2006). The biogenic VOC and NO emissions were calculated online by using the Model of Emissions of Gases and Aerosols from Nature (MEGAN) that embedded in WRF-Chem (Guenther et al., 2006). More than 20 biogenic species, including isoprene, monoterpenes (e.g., α -pinene and β -pinene) and sesquiterpenes, were considered and then involved in the photochemistry calculation. In China, crop residues are usually burned in piles, which is characterized by short-lived and small-scale smoldering. Consequently, the plume rise of biomass burning plumes was not considered in this study, and the straw fire emission was placed in the lowest two levels from the surface to around 50 meter in this simulation.

Previous studies have shown that, under highly polluted conditions, the ARI dominated over the aerosol-cloud interaction (ACI) that is related to aerosols' ability to act as CCN (e.g., Rosenfeld et al., 2008; Fan et al., 2015). We also conducted another numerical experiment which included both ACI and ARI. The ACI-induced radiative perturbations were much less notable than those caused by ARI both at the surface and in the atmosphere (Figure S2), implying the dominant role of ARI during this fire event. Since that the focus of this study is on ARI and ACI's effect was not that significant, the prognosed aerosol was disabled to act as cloud condensation nuclei (CCN) or ice nuclei (IN) in the simulations and therefore the effects from ACI were not accounted for in the following analysis. Accordingly, wet scavenging of aerosol was disabled too. In order to disentangle aerosols' role in radiative transfer and subsequent effects on cloud and precipitation during this biomass-burning event in the mid-June of 2012, we designed three parallel numerical experiments. Domain settings and model configurations for these simulations were exactly the same as mentioned before. The control

experiment (CTL) did not include aerosol's effects on either longwave or shortwave radiation transfer. On the contrary, the other two took account of aerosols' perturbations on radiation transfer: ARI-A with anthropogenic emissions (anthropogenic activities refer to power generation, transportation, industrial and residential activities hereafter) and ARI-AB that included both anthropogenic activities and biomass burning emissions.

3 Results and discussions

3.1 Fire-induced pollution and observed anomalies in meteorology

As demonstrated by existing studies (Andreae et al., 1988; Huang et al., 2012c; Ding et al., 2013a), air quality was dramatically deteriorated and the visibility was impeded during biomass burning events. We compare the simulated daily averaged PM_{10} concentration with the corresponding measurements derived from Air Pollution Index (API) in Figure 3 (If not mentioned specially, the simulation refers to ARI-AB experiment hereafter). Both observations and simulations manifested the fact that intensive agricultural fires led to the severe pollution in mid-June. Since 9 June when the detected fire spots became intense and extensive, PM_{10} concentrations in northern Anhui and northwest Jiangsu province began to increase, especially for those regions near the fire location. For instance, the observed daily mean PM_{10} concentrations reached up to around $250 \mu g/m^3$ at Fuyang (FY) and Xuzhou (XZ) and even exceeded $400 \mu g/m^3$ at Bengbu (BB) on 9 June (the locations of cities mentioned in this article are labelled in Figure 2). Although the simulated temporal variations agree with observations, model-predicted PM_{10} concentration at FY and BB were 196 and $168 \mu g/m^3$, respectively. The underestimation might be due to that rapid formation of secondary aerosol like sulfate and secondary organic matters is not so well described in current atmospheric chemical transport models (Capes et al., 2008; Xie et al., 2015). XZ and BB suffered from the second-round fire smoke two days later, with a maximum daily mean concentration of $548 \mu g/m^3$ observed at BB. Figure 4 illustrates the satellite-retrieved 660-nm aerosol optical depth (AOD) and SSA from MODIS Aerosol Product MOD04_L2 (daily level 2 data produced at the spatial resolution of 10 km, collection 6) around 11:00 local time (LT) on 9 June when the first-round of extensive fire pollution broke out. Their comparisons with ARI-AB modelled spatial distributions of $PM_{2.5}$ and BC column-integrated mass loadings further confirm model's ability to reproduce atmospheric pollution for this event. The AOD observation shows that high aerosol loadings were concentrating in northeast Anhui and the north-central Jiangsu, shaping a belt of pollution from the fire sites to the downwind areas. The similar pattern was also simulated by the model.

The PM_{2.5} mass loading was found to exceed 200 mg/m² near BB, NJ and most parts of central Jiangsu. This strap-shaped pollution was particularly obvious in terms of BC column concentrations, which was also consistent with a relatively lower SSA along BB, Yangzhou (YZ) and Taizhou (TZ). While solely including anthropogenic emissions, ARI-A experiment failed to represent the spatial pattern of high AOD in the northern Anhui and Jiangsu and the low SSA value near BB (Fig.4 a, d).

Along with the severe air pollution and poor visibility, anomalies in meteorology occurred on 9-10, June. Ding et al. (2013a) found that, during these two days, a sharp decline existed in the observed air temperature in NJ and YZ, compared with weather forecast results and NCEP FNL data, but the simulations and observations showed a good agreement when the heavy air pollution was not present before 8 June. At YZ the temperature difference was as high as 5.9 and 9.2 °C on 9 and 10 June, respectively. Simultaneously, measured solar radiation intensity and sensible heat flux showed very low values on 10 June in comparison with non-episode days. Moreover, local meteorological agency forecasted a convective rainfall to occur in NJ and surrounding areas in the afternoon of 10 June, with the rainfall centre passing by NJ around 14:00 LT. However, this forecasted rainfall never happened that day.

On the basis of ground-based measurements, vertical sounding data, remote-sensing images and their comparisons with numerical simulations, we found that agricultural fires worsen regional air quality to a large extent and caused a series of anomalies in temperature and precipitation in the mid-June of 2012. How the biomass burning plumes influenced the air temperature and precipitation will be the main issue to be addressed in the following discussions.

3.2 Perturbations in energy budget and temperature responses

To better understand aerosols' role in the energy re-allocation on 10 June when precipitation was evidently modified, radiative forcing in the atmosphere and at the ground surface was estimated by differentiating the CTL, ARI-A and ARI-AB simulations (Figure 5). At the surface, daily mean incident short-wave radiation was weakened by 45.5 W/m² (averaged over the inner domain) as the extinction of aerosol was quite large with a satellite-observed 660-nm AOD exceeding 2.0 (Figure 4b). Meanwhile, about 60.4 W/m² shortwave energy was blocked in the atmosphere over the inner domain due to the fact that absorbing aerosols were accumulated on that day. A positive domain-averaged radiative forcing of +14.9 W/m² was simulated at the top of the atmosphere (TOA) on 10 June. Comparatively, radiative perturbations caused by

agricultural fires (ARI-AB minus ARI-A) were more substantial than those due to anthropogenic emissions (ARI-A minus CTL) in magnitude, particularly in the atmosphere, as presented in Figure 5. Spatially, radiative effects due to anthropogenic activities concentrated in the economically developed Yangtze River Delta region while agricultural fires exerted significant impact on radiation balance in northern and central Jiangsu and north part of Anhui. Table 2 compares the radiative perturbations caused by anthropogenic activities and biomass burning emissions over three regions with distinct precipitation changes (marked in Figure 8). As shown, both of them tended to heat the atmosphere and cool the ground surface. Fire plumes dominated the radiative effect in terms of atmospheric warming. Radiation measurements collected at Heifei (HF) and sensible and latent heat flux recorded at Lishui (in South Nanjing) are compared with the diurnal variations of corresponding simulations in Figure 6, which supports that significant radiative perturbations took place at NJ and HF. Substantially weakened daytime solar irradiance was observed on 10 June, when the peak value of downwelling shortwave radiation was 618.3 W/m^2 at HF and was only 309.7 W/m^2 at NJ. Taking aerosol's effect on radiation into account tended to predict lower downwards solar radiation, which was closer to observation for both cities. Reduction in shortwave energy hitting the surface in turn decreased outgoing heat fluxes, and therefore simulated sensible and latent heat fluxes at 12:00 LT on 10 June in ARI-AB experiment decreased by 89.3 and 76.1 W/m^2 , respectively, compared with CTL experiment.

Overall, the magnitude of the radiative forcing on 10 June was comparable in northern Anhui and central Jiangsu, differing from the distribution pattern of fire-induced air pollution that remarkably concentrated in northern Anhui. As revealed in our previous estimation, among all components of the ambient aerosols, BC is the most important disturber of shortwave radiation transfer at the surface and in the atmosphere as well (Huang et al., 2015; Ding et al., 2016). Although fire emission mostly concentrated in the northern Anhui and resulted in a high BC concentration of $20 \mu\text{g/m}^3$ there, high-altitude BC was spread much more broadly. At an altitude of 2 km, BC concentration around $5 \mu\text{g/m}^3$ stretched from northern Anhui to central Jiangsu (Figure S3). Such distinct distributions between two layers were partly attributed to the stagnant condition near the surface and stronger horizontal transport in the upper level. It is emphasized that upper-level BC has higher absorbing efficiency (Ding et al., 2016). That is why the distributions of both positive radiative forcing in the atmosphere and negative forcing at the surface generally consisted with BC's spatial pattern in the upper air.

The perturbations in the energy budget and the following re-allocation gave rise to substantial modulation in vertical stratification of air temperature. In comparison with CTL experiment, ARI-AB experiment predicted an obvious decline in near-surface temperature by considering the effects of aerosol-radiation interaction. Hourly observed 2-m air temperature was compared with corresponding simulations by two experiments during the time period from 8 to 15 June. Model-performance statistics including mean bias (MB), mean error (ME) and root mean square error (RMSE) are presented in Table 3. As shown, CTL simulation had a systematic positive bias in 2-m temperature and ARI predicted lower temperature for both areas near fire locations (BB and XZ) and downwind regions (NJ and SY). The decreases in temperature were pronounced in BB and XZ with a large difference of approximately 1.2 °C, which notably narrowed the gaps with observations. On 10 June when the fire-induced pollution became intensive, the magnitude of surface cooling was remarkably high near the fire sites. Temperature response in Figure 5e support this cooling effect. For instance, compared to CTL, simulated near-surface temperature by ARI-A and ARI-AB experiment at XZ was cooled by almost 1.2 and 8.0 °C at 20:00 LT on 10 June (Figure 7b). In addition to the cooling tendency of near-surface temperature, aerosols' radiative effects also increased air temperature at a higher altitude, which were more apparent over the downwind areas (Figure 5f). According to the comparisons between simulated temperature profiles by the three parallel experiments in Figure 7, the warming of air temperature was particularly evident around an altitude of 2 km at SY with a maximum of 3.0 °C and biomass burning aerosol played a leading role.

The different temperature responses over the source region of fire emission and downwind areas could be partially interpreted by the fact that near the fire locations, pronounced surface cooling counteracted part of the atmospheric warming, which would otherwise elevate upper-air temperature, through vertical mixing; while for the downwind area where the surface was less radiatively cooled, the atmosphere was prone to being warmed. As a result of surface cooling and atmospheric heating, vertical convective motions were weakened, triggering perturbations in pressure and wind fields (Figure 5e and f). It is obvious that suppressed convection was generally along with the resultant wind convergence around 2 km and surface divergence, which may further play a significant role in water vapor transport, entrainment and also cloud formation.

3.3 Effects on cloud and precipitation

In addition to the attenuation of solar radiation and the modulation in temperature gradients, precipitation also showed many disparities between CTL and ARI-AB simulations. The satellite observation from Tropical Rainfall Measuring Mission (TRMM) Multisatellite Precipitation Analysis product (3B42), which provides merged-infrared precipitation information at a $0.25 \times 0.25^\circ$ spatial resolution and has been demonstrated to perform well in East China (Simpson et al., 1988; Zhao and Yatagai, 2014), was used to evaluate the simulated precipitation. As demonstrated in Figure 8, ARI-AB experiment agrees better with TRMM observations than CTL experiment in terms of precipitation intensities and also spatial pattern on 10 June. Specifically, CTL and ARI-A simulation suggested a convective rain in Zone 1 (NJ and its adjacent areas) around 14:00 LT (the locations of Zone 1-3 are marked in Figure 8), however the ARI-AB simulation did not show any precipitation then, consistent with the TRMM observations. Besides, ARI-AB displayed enhanced precipitation in northern Jiangsu province. A precipitation with the intensity of 3 and 5 mm/h was predicted by ARI-AB experiment in Zone 2 (XZ and its adjacent areas) and Zone 3 (SY and its adjacent areas), which, however, never occurred in CTL and ARI-A experiment. Concerning temporal variations, 3-hour precipitation rates for these three zones derived from TRMM 3B42 retrievals are plotted in Figure 9. Compared to CTL and ARI-A experiment, ARI-AB experiment which considered radiative effects of aerosol from both anthropogenic and biomass burning emissions succeeded in capturing the approximate onset time for all the three regions.

3.3.1 Suppressed daytime precipitation

Over Zone 1, CTL and ARI-A simulation produced a convective rainfall event in the afternoon that actually did not happen, while ARI-AB simulation with no precipitation was closer to the observations. According to the energy budget and radiation flux calculation (Figure 5), on 10 June more than 6 MJ/m^2 solar radiation that supposed to reach the surface was blocked in the atmosphere over Zone 1, most of which was caused by biomass burning aerosol. The presence of light-absorbing aerosols reduced sensible heat flux and evapotranspiration at the surface (Figure 6). Large-eddy simulation for biomass burning regions of Brazil deduced that the peak reductions in sensible and latent heat flux were 60 and 70 W/m^2 (Feingold et al., 2005), which are quantitatively similar to those near NJ estimated in this work. It was shown that reduced surface flux alone was sufficient to explain the observed cloud dissipation during the biomass burning event in Brazil. For this case, this convective rain got disappeared merely by nudging

2-m temperature in the WRF modelling run by Ding et al. (2013a), highlighting the importance of surface flux modification in the development of these convective clouds.

To figure out the role of vertical thermal behaviors in Zone 1, temporal variations of zone-averaged differences in temperature, relative humidity (RH) profiles between ARI-AB and CTL experiments are illustrated in Figure 10a and b. From 9:00 LT in the morning, a 1-km-thick belt with BC-laden smoke approached Zone 1 and covered over the boundary layer top. The radiative extinction by the elevated smoke layer led to a cooling effect at the surface, which reduced the boundary layer height and decreased the air temperature in the boundary layer. Simultaneously, relatively strong warming effect between the altitudes of 1-3 km increased the air temperature above the boundary layer. The cooling at the lower altitude and warming at the upper altitude made the stability significantly increased, especially near the top of the boundary layer, which further suppressed the development of boundary layer. For the perturbations in humidity, the enhanced atmospheric stability reduced the boundary layer height and hindered the upward transport of water vapor to a higher altitude, while the heating aloft decreased RH by increasing the air temperature there. These led to a resultant decrease of more than 20% in RH above the boundary layer. A more stable and shallower boundary layer in ARI-AB experiment had a tendency to reduce convective mixing and effectively cut off the cloud layer from its source of moisture, subsequently desiccating the cloud layer, and leading to substantially weakened vertical motions. Accordingly, ARI-AB simulated updraft velocity above 1 km was only one-tenth that of CTL experiment in the afternoon of 10 June, as demonstrated in Figure 10f. Even though anthropogenic aerosol also weakened convective motions in ARI-A experiment, the potential temperature profile was hardly changed and the weakening effect of convection was not comparable with that caused by biomass burning aerosols. Therefore, compared with CTL and ARI-A experiment, much less moist static energy (MSE) was carried upwards and the excess MSE accumulated in a shallower boundary layer due to much weaker convection in ARI-AB experiment (Figure 10e).

In addition to Zone 1, this warmed belt was also blanketing a wider range from 116 to 120 °E at the moment when the CTL-predicted rainfall started (Figure 9a shows that the rainfall occurred around 14:00 LT), as shown in the longitude-height cross sections of temperature difference between CTL and ARI-AB experiment in Figure 10c. In CTL run, cumulus cloud layer appeared above the inversion capping the boundary layer (Figure 10d). However, the absorbing aerosol in ARI-AB run heated the atmosphere aloft and stabilized the sub-cloud layer.

The decrease in specific humidity was collocated with warmed upper air since that atmospheric heating and surface cooling weakened vertical convection and further reduced the vertical transport of water vapor. Lower entrainment rate together with higher saturation pressure resulted in daytime decoupling and thinning of the cloud layer all along the longitude from 116 to 120 °E. This effect might be further strengthened by a positive feedback loop as described by Jacobson (2002) in which cloud loss leads to an increasing opportunity for BC's light absorption.

3.3.2 Enhanced nocturnal precipitation

A precipitation rate of over 2.5 mm/h was observed around 19:00-20:00 LT on 10 June in XZ and its surrounding areas (Zone 2). Only ARI-AB simulation captured this precipitation event. As shown in Figure 11a, there existed two layers with a high BC concentration of up to 10 $\mu\text{g}/\text{m}^3$ during daytime over Zone 2. One was near the surface and peaked around 18:00 LT, which could be linked to local fire emissions. The other one was lying over the boundary layer top, which was apparent at an altitude of 0.8 km before the boundary layer developed and at 2 km after 15:00 LT. It was very likely to be associated with the transport of upstream fire pollution. Owing to strong radiative heating effect of BC, a warmer layer was formed above 1 km during daytime with temperature increase over 1.0 °C. On the contrary, near-surface temperature kept decreasing. The decline reached its maximum around 20:00 LT. It was also supported by Figure 7b in which the near-surface temperature decreased by almost 8.0 °C at XZ. Until 16:00 LT, the upper-air warming due to radiative absorption was gradually compensated by cooling from the surface through vertical mixing. Changes in RH were almost opposite of those in air temperature. Around 18:00 LT, RH at 3-km altitude started to increase and then a precipitating cloud formed there.

To get a better insight on the dynamical processes that contribute to precipitation change, longitude-height cross section of zonal mean responses of temperature, water vapor and wind profile just before the onset time of precipitation are demonstrated in Figure 11c and d. Noteworthy is that warmed upper air between 117 to 119 °E led to less condensation there. More water vapor accumulated below 1 km and was then transported toward Zone 2 by the prevailing east wind near the surface, leading to an excess water vapor over Zone 2 in [ARI-AB experiment](#) (Figure 11e). Simultaneously, radiatively heated air parcel with a temperature increase of 0.5 °C was found around 2 km over Zone 2. The warmer layer around 2-3 km combined with large drops in temperature beneath resulted in a buoyancy-driven lifting force.

Moreover, horizontal heterogeneity in atmospheric heating provided the low-level convergence for maintaining convection in a conditionally unstable atmosphere around 3 km. The zone-averaged updraft velocity in ARI-AB experiment tripled that predicted by CTL and ARI-A at the altitude of 3 km when the precipitation began (Figure 11f). Understandably, what made the precipitating cloud formed around 3 km over Zone 2 were the accumulated MSE near the surface and anomalous updraft of the air that favored the vertical uplift of MSE. The release of latent heat may increase the upper-air instability and in turn enhance the precipitation.

For the downwind region Zone 3, the warming effect caused by aerosol-radiation interaction was evident for the air column above 0.5 km all day long on 10 June (Figure 12a). The warming pattern was coincident with the distribution of BC concentration since BC is the predominant light-absorbing aerosol specie in the atmosphere. As a result of increased air temperature, RH decreased substantially during daytime. At late night, an extra precipitating cloud formed above 2 km over Zone 3 in ARI-AB simulation, leading to a nocturnal precipitation with a strength of approximately 6 mm/h at 01:00 LT on 11 June. What triggered this rainfall event is a bit complicated than that over Zone 2. First, the whole air column was getting cooled at the moment when the precipitation took place, inevitably raising RH value. The RH increase was quite apparent at the altitude of 3-4 km. Second, daytime radiative absorption by BC-laden plumes around 2 km heated the surrounding air. Relatively warmer layer at the altitude of ~ 2 km generated a positive buoyant updraft (Figure 12f), hence air parcel there was displaced upwards along with enhanced convergence carrying in moist air. This effect has been proposed by Fan et al. (2015) as part of termed “enhanced conditional instability”, by which absorbing aerosols escalate convection downwind of a heavily polluted area and promote precipitation. Comparatively, radiative heating of biomass burning aerosol was the main contributor to the significant enhancement of upper-level updraft. Last but not the least, spatially heterogeneous aerosol-related heating was associated with greater horizontal temperature lapse, resulting in a convergence flow above 3 km with an additional onshore wind (Figure 12d). Zone 3 is only about 20 km from the Yellow sea. It is plausible that more water vapor-saturated air masses originating from the ocean brought in excess water vapor and consequently elevated the humidity above 3 km. More MSE accumulated above 3 km in ARI-AB experiment compared with those simulated by CTL and ARI-A experiment before the precipitation also support this view (Figure 12e). We suggest that these precipitating clouds formed because of instability at the top of the smoke layer, driven by the strong radiation absorption that warmed the

surrounding air. Therefore, the heated BC-laden air was ascended and cooled, leading to the formation of clouds preferentially in the conditionally unstable zone in the upper air.

3.4 Uncertainties

Though the modelling work here characterized cloud and precipitation anomalies during the biomass burning event, we may also question to what extent the modelling reproduced the relevant processes in the real world. As widely acknowledged, accurate simulation of smoke plume and prediction of clouds are both challenging for regional/global models. One contributor to the uncertainties is the characterization of fire emission. The magnitude was determined by statistical information and laboratory experiment data, whose accuracy and representativeness may introduce some uncertainties. The spatiotemporal distribution of fire emission was allocated based on MODIS retrievals. Loss of information due to cloud coverage and poor detection efficiency of short-lived or small-scale fires are major limitations (Giglio et al., 2003). Another challenge is quantification of heat release from biomass burning and subsequent effects on local and regional meteorology. Furthermore, much emphasis has been paid to the vertical distribution of absorbing aerosol, to which the cloud response is highly sensitive (Koch and Del Genio, 2010). The vertical profile of absorbing aerosol in this simulation underwent little constrain due to limited observation at that time. The regional model is hardly capable of precisely presenting turbulent flows and vertical transport, thus introducing uncertainties in three dimensional distributions of BC. It also should be noted that BC is co-emitted with other components such as OC and sulfur dioxide that oxidizes to sulfate (Xie et al., 2015). Mixing with other scattering aerosol would considerably amplify the absorbing efficiency of BC. Model's ability to account for the evolution of mixing state and how to quantify its amplification also affect the simulated radiative behaviors. Besides, poorly recognized secondary organic carbon (SOC) formation processes and its light absorption makes it imperative to reassess and redefine the chemical mechanism and optical properties of OC in models (Saleh et al., 2014). The large uncertainty in simulating clouds and further aerosol-cloud interaction is another limitation (e.g., Wang et al., 2011; Tao et al., 2012). To improve the model performance in all these chemical and physical processes, more comprehensive measurements and modelling efforts are needed in the future.

4 Conclusions

To investigate radiative effects of aerosol-radiation interaction on cloud and precipitation modifications during the exceptionally active agricultural fire season in June 2012, a bottom-up emission inventory of crop open burning was developed and then the fully coupled online WRF-Chem model was applied in this work. The evaluation of simulation through ground-based observations and satellite retrievals showed that the model generally captured spatial patterns and temporal variations of fire pollution, which was predominantly concentrating over northern Anhui and central-north Jiangsu. It is evident that post-harvest burning of crop residues emitted a tremendous amount of atmospheric pollutants and deteriorated regional air quality to a large extent in East China. Elevated concentration of aerosols, particularly light-absorbing BC, would heat the atmosphere and cool the ground surface through both direct solar radiation attenuation (direct radiative forcing) and cloud redistribution (semi-direct radiative forcing). This radiative cooling (heating) effects were distinct close to (downwind from) the source regions of fire sites. Adjusted temperature stratification was intimately linked to small-scale processes such as turbulent mixing, entrainment and the evolution of the boundary layer. Subsequently, over Nanjing and its adjacent regions, absorbing aerosols immediately above the boundary layer top increased the inversion beneath, reducing available moisture and leading to a burn-off effect of cloud. Meanwhile, fire plumes played an enhancement role in nocturnal precipitation over northern Jiangsu by increasing up-level convective activity and fostering low-level convergence that carries in more moist air. Overall, aerosols' radiative effect on precipitation modification is therefore likely to depend to a large extent on local meteorological conditions like atmospheric instability and humidity.

Acknowledgements

This work was supported by the National Natural Science Foundation of China (D0512/91544231, D0512/41422504, and D0510/41505109). Part of this work was supported by the Jiangsu Provincial Science Fund for Distinguished Young Scholars awarded to A. J. Ding (No. BK20140021).

1 Table 1. WRF-Chem modelling configuration options and settings.

Domain setting		
	Domain 1	Domain 2
Horizontal grid	130×130	160×160
Grid spacing	20 km	4 km
Vertical layers	31	31
Configuration options		
Long-wave radiation	RRTMG	
Short-wave radiation	RRTMG	
Land-surface	Noah	
Boundary layer	YSU	
Microphysics	Lin et al.	
Cumulus parameterization	Grell–Deveny (only for domain 1)	
Photolysis	Fast-J	
Gas-phase chemistry	CBMZ	
Aerosol scheme	MOSAIC	

2

3

Table 2. Radiative perturbations at the surface (SUR) and in the atmosphere (ATM) caused by anthropogenic activities and agricultural fires for three zones with distinct precipitation changes.

	SUR		ATM	
	Anthropogenic activities	Agricultural fires	Anthropogenic activities	Agricultural fires
Zone 1	-27.3	-35.1	36.3	41.1
Zone 2	-33.3	-41.7	31.9	45.6
Zone 3	-23.8	-14.8	27.7	21.1

Table 3. Statistical analyses of the simulated 2-m temperature and the corresponding observations at four different cities.

	MB ^a		ME ^a		RMSE ^a	
	CTL	ARI	CTL	ARI	CTL	ARI
NJ	0.85	0.37	1.70	1.66	2.39	2.15
BB	2.19	0.98	2.51	1.65	3.27	2.16
XZ	1.67	0.51	2.37	2.19	3.32	2.89
SY	-0.28	-0.46	1.97	1.65	2.52	2.03

^aMB, ME and RMSE refer to mean bias, mean error and root-mean-square error respectively.

1 **References**

- 2 Akagi, S. K., Yokelson, R. J., Wiedinmyer, C., Alvarado, M. J., Reid, J. S., Karl, T., Crounse,
3 J. D., and Wennberg, P. O.: Emission factors for open and domestic biomass burning for use in
4 atmospheric models, *Atmos. Chem. Phys.*, 11, 4039-4072, 10.5194/acp-11-4039-2011, 2011.
- 5 Andreae, M. O., Browell, E. V., Garstang, M., Gregory, G. L., Harriss, R. C., Hill, G. F., Jacob,
6 D. J., Pereira, M. C., Sachse, G. W., Setzer, A. W., Dias, P. L. S., Talbot, R. W., Torres, A. L.,
7 and Wofsy, S. C.: Biomass-Burning Emissions and Associated Haze Layers over Amazonia, *J.*
8 *Geophys. Res. Atmos.*, 93, 1509-1527, doi:10.1029/Jd093id02p01509, 1988.
- 9 Andreae, M. O., and Merlet, P.: Emission of trace gases and aerosols from biomass burning,
10 *Global Biogeochem. Cy.*, 15, 955-966, doi:10.1029/2000gb001382, 2001.
- 11 Andreae, M. O., Rosenfeld, D., Artaxo, P., Costa, A. A., Frank, G. P., Longo, K. M., and Silva-
12 Dias, M. A. F.: Smoking rain clouds over the Amazon, *Science*, 303, 1337-1342,
13 doi:10.1126/science.1092779, 2004.
- 14 Barnard, J. C., Fast, J. D., Paredes-Miranda, G., Arnott, W. P., and Laskin, A.: Technical Note:
15 Evaluation of the WRF-Chem "Aerosol Chemical to Aerosol Optical Properties" Module using
16 data from the MILAGRO campaign, *Atmos. Chem. Phys.*, 10, 7325-7340, 10.5194/acp-10-
17 7325-2010, 2010.
- 18 Bergamaschi, P., Hein, R., Heimann, M., and Crutzen, P. J.: Inverse modeling of the global CO
19 cycle 1. Inversion of CO mixing ratios, *J. Geophys. Res. Atmos.*, 105, 1909-1927,
20 doi:10.1029/1999jd900818, 2000.
- 21 Berge, E., Huang, H. C., Chang, J., and Liu, T. H.: A study of the importance of initial
22 conditions for photochemical oxidant modeling, *J. Geophys. Res. Atmos.*, 106, 1347-1363,
23 doi:10.1029/2000jd900227, 2001.
- 24 Bond, T. C., Doherty, S. J., Fahey, D. W., Forster, P. M., Berntsen, T., DeAngelo, B. J., Flanner,
25 M. G., Ghan, S., Karcher, B., Koch, D., Kinne, S., Kondo, Y., Quinn, P. K., Sarofim, M. C.,
26 Schultz, M. G., Schulz, M., Venkataraman, C., Zhang, H., Zhang, S., Bellouin, N., Guttikunda,
27 S. K., Hopke, P. K., Jacobson, M. Z., Kaiser, J. W., Klimont, Z., Lohmann, U., Schwarz, J. P.,
28 Shindell, D., Storelvmo, T., Warren, S. G., and Zender, C. S.: Bounding the role of black carbon
29 in the climate system: A scientific assessment, *J. Geophys. Res. Atmos.*, 118, 5380-5552,
30 10.1002/jgrd.50171, 2013.
- 31 Boschetti, L., Roy, D., and Hoffmann, A.: MODIS Collection 5 Burned Area Product-MCD45,
32 User's Guide, Ver, 2, 2009.
- 33 Capes, G., Johnson, B., McFiggans, G., Williams, P., Haywood, J., and Coe, H.: Aging of
34 biomass burning aerosols over West Africa: Aircraft measurements of chemical composition,
35 microphysical properties, and emission ratios, *J. Geophys. Res. Atmos.*, 113, 2008.
- 36 Chi, X., Winderlich, J., Mayer, J.-C., Panov, A. V., Heimann, M., Birmili, W., Heintzenberg,
37 J., Cheng, Y., and Andreae, M. O.: Long-term measurements of aerosol and carbon monoxide
38 at the ZOTTO tall tower to characterize polluted and pristine air in the Siberian taiga, *Atmos.*
39 *Chem. Phys.*, 13, 12271-12298, doi:10.5194/acp-13-12271-2013, 2013.
- 40 Crutzen, P. J., and Andreae, M. O.: Biomass Burning in the Tropics - Impact on Atmospheric
41 Chemistry and Biogeochemical Cycles, *Science*, 250, 1669-1678, doi:10.1126/science.250.
42 4988.1669, 1990.

1 Ding, A. J., Fu, C. B., Yang, X. Q., Sun, J. N., Petaja, T., Kerminen, V. M., Wang, T., Xie, Y.,
2 Herrmann, E., Zheng, L. F., Nie, W., Liu, Q., Wei, X. L., and Kulmala, M.: Intense atmospheric
3 pollution modifies weather: a case of mixed biomass burning with fossil fuel combustion
4 pollution in eastern China, *Atmos. Chem. Phys.*, 13, 10545-10554, 10.5194/acp-13-10545-
5 2013, 2013a.

6 Ding, A. J., Fu, C. B., Yang, X. Q., Sun, J. N., Zheng, L. F., Xie, Y. N., Herrmann, E., Nie, W.,
7 Petaja, T., Kerminen, V. M., and Kulmala, M.: Ozone and fine particle in the western Yangtze
8 River Delta: an overview of 1 yr data at the SORPES station, *Atmos. Chem. Phys.*, 13, 5813-
9 5830, 10.5194/acp-13-5813-2013, 2013b.

10 Ding, A. J., Huang, X., Nie, W., Sun, J. N., Kerminen, V. M., Petäjä, T., Su, H., Cheng, Y. F.,
11 Yang, X. Q., Wang, M. H., Chi, X. G., Wang, J. P., Virkkula, A., Guo, W. D., Yuan, J., Wang,
12 S. Y., Zhang, R. J., Wu, Y. F., Song, Y., Zhu, T., Zilitinkevich, S., Kulmala, M., and Fu, C. B.:
13 Enhanced haze pollution by black carbon in megacities in China, *Geophys. Res. Lett.*,
14 doi:10.1002/2016GL067745, 2016.

15 Draxler, R. R., and Rolph, G.: HYSPLIT (HYbrid Single-Particle Lagrangian Integrated
16 Trajectory) model access via NOAA ARL READY website (<http://www.arl.noaa.gov/ready/hysplit4.html>). NOAA Air Resources Laboratory, Silver Spring, in, Md, 2003.

18 Ek, M. B., Mitchell, K. E., Lin, Y., Rogers, E., Grunmann, P., Koren, V., Gayno, G., and
19 Tarpley, J. D.: Implementation of Noah land surface model advances in the National Centers
20 for Environmental Prediction operational mesoscale Eta model, *J. Geophys. Res. Atmos.*, 108,
21 Artn 8851, doi:10.1029/2002jd003296, 2003.

22 Fan, J. W., Rosenfeld, D., Yang, Y., Zhao, C., Leung, L. R., and Li, Z. Q.: Substantial
23 contribution of anthropogenic air pollution to catastrophic floods in Southwest China, *Geophys.*
24 *Res. Lett.*, 42, 6066-6075, 10.1002/2015GL064479, 2015.

25 Fast, J. D., Gustafson, W. I., Easter, R. C., Zaveri, R. A., Barnard, J. C., Chapman, E. G., Grell,
26 G. A., and Peckham, S. E.: Evolution of ozone, particulates, and aerosol direct radiative forcing
27 in the vicinity of Houston using a fully coupled meteorology-chemistry-aerosol model, *J.*
28 *Geophys. Res. Atmos.*, 111, Artn D21305, doi:10.1029/2005jd006721, 2006.

29 Fearnside, P. M.: Global warming and tropical land-use change: greenhouse gas emissions from
30 biomass burning, decomposition and soils in forest conversion, shifting cultivation and
31 secondary vegetation, *Climatic change*, 46, 115-158, 2000.

32 Feingold, G., Jiang, H. L., and Harrington, J. Y.: On smoke suppression of clouds in Amazonia,
33 *Geophys. Res. Lett.*, 32, Artn L02804, doi:10.1029/2004gl021369, 2005.

34 Gao, M., Carmichael, G., Wang, Y., Saide, P., Yu, M., Xin, J., Liu, Z., and Wang, Z.: Modeling
35 study of the 2010 regional haze event in the North China Plain, *Atmospheric Chemistry &*
36 *Physics*, 16, 2016.

37 Gao, X., Ma, W., Ma, C., Zhang, F., and Wang, Y.: Analysis on the current status of utilization
38 of crop straw in China (in Chinese), *Journal of Huazhong Agricultural University*, 21, 242-247,
39 2002.

40 Giglio, L., Descloitres, J., Justice, C. O., and Kaufman, Y. J.: An enhanced contextual fire
41 detection algorithm for MODIS, *Remote. Sens. Environ.*, 87, 273-282, 10.1016/S0034-
42 4257(03)00184-6, 2003.

1 Grell, G., Freitas, S. R., Stuefer, M., and Fast, J.: Inclusion of biomass burning in WRF-Chem:
2 impact of wildfires on weather forecasts, *Atmos. Chem. Phys.*, 11, 5289-5303, 10.5194/acp-
3 11-5289-2011, 2011.

4 Grell, G. A., and Devenyi, D.: A generalized approach to parameterizing convection combining
5 ensemble and data assimilation techniques, *Geophys. Res. Lett.*, 29, Artn 1693, doi:
6 10.1029/2002gl015311, 2002.

7 Guenther, A., Karl, T., Harley, P., Wiedinmyer, C., Palmer, P. I., and Geron, C.: Estimates of
8 global terrestrial isoprene emissions using MEGAN (Model of Emissions of Gases and
9 Aerosols from Nature), *Atmos. Chem. Phys.*, 6, 3181-3210, 2006.

10 Hong, S. Y.: A new stable boundary-layer mixing scheme and its impact on the simulated East
11 Asian summer monsoon, *Q. J. Roy. Meteor. Soc.*, 136, 1481-1496, doi:10.1002/Qj.665, 2010.

12 Hsu, Y., Strait, R., Roe, S., and Holoman, D. S.: 4.0. Speciation Database Development
13 Documentation. Final Report. EPA contract. Nos, EP-D-06.001, work assignment Numbers 0-
14 03 and 68-D-02-063, WA 4-04 and WA 5-05. EPA/600/R-06/16. [http://www.epa.](http://www.epa.gov/ttn/chief/software/speciate/speciate4/documentation/speciatedoc_1206.pdf)
15 [gov/ttn/chief/software/speciate/speciate4/documentation/speciatedoc_1206.pdf](http://www.epa.gov/ttn/chief/software/speciate/speciate4/documentation/speciatedoc_1206.pdf), 2006.

16 Huang, X., Song, Y., Li, M., Li, J., Huo, Q., Cai, X., Zhu, T., Hu, M., and Zhang, H.: A high -
17 resolution ammonia emission inventory in China, *Global Biogeochem. Cy.*, 26, 2012a.

18 Huang, X., Li, M. M., Li, J. F., and Song, Y.: A high-resolution emission inventory of crop
19 burning in fields in China based on MODIS Thermal Anomalies/Fire products, *Atmos. Environ.*,
20 50, 9-15, 10.1016/j.atmosenv.2012.01.017, 2012b.

21 Huang, X., Song, Y., Li, M. M., Li, J. F., and Zhu, T.: Harvest season, high polluted season in
22 East China, *Environ. Res. Lett.*, 7, Artn 044033, doi:10.1088/1748-9326/7/4/044033, 2012c.

23 Huang, X., Song, Y., Zhao, C., Cai, X. H., Zhang, H. S., and Zhu, T.: Direct Radiative Effect
24 by Multicomponent Aerosol over China, *J. Climate*, 28, 3472-3495, 10.1175/Jcli-D-14-00365.1,
25 2015.

26 Ito, A., Ito, A., and Akimoto, H.: Seasonal and interannual variations in CO and BC emissions
27 from open biomass burning in Southern Africa during 1998-2005, *Global Biogeochem. Cy.*, 21,
28 Artn Gb2011, doi:10.1029/2006gb002848, 2007.

29 Jacobson, M. Z.: Control of fossil-fuel particulate black carbon and organic matter, possibly the
30 most effective method of slowing global warming, *J. Geophys. Res. Atmos.*, 107, Artn 4410,
31 doi:10.1029/2001jd001376, 2002.

32 Koch, D., and Del Genio, A. D.: Black carbon semi-direct effects on cloud cover: review and
33 synthesis, *Atmos. Chem. Phys.*, 10, 7685-7696, 10.5194/acp-10-7685-2010, 2010.

34 Kolusu, S. R., Marsham, J. H., Mulcahy, J., Johnson, B., Dunning, C., Bush, M., and Spracklen,
35 D. V.: Impacts of Amazonia biomass burning aerosols assessed from short-range weather
36 forecasts, *Atmos. Chem. Phys.*, 15, 12251-12266, 10.5194/acp-15-12251-2015, 2015.

37 Koren, I., Kaufman, Y. J., Remer, L. A., and Martins, J. V.: Measurement of the effect of
38 Amazon smoke on inhibition of cloud formation, *Science*, 303, 1342-1345, doi: 10.1126
39 /science.1089424, 2004.

40 Krishnan, R., and Ramanathan, V.: Evidence of surface cooling from absorbing aerosols,
41 *Geophys. Res. Lett.*, 29, Artn 1340, doi:10.1029/2002gl014687, 2002.

42 Kuhlbusch, T. A. J.: Black carbon and the carbon cycle, *Science*, 280, 1903-1904,
43 doi:10.1126/science.280.5371.1903, 1998.

1 Kulmala, M., Lappalainen, H.K., Petäjä, T., Kurten, T., Kerminen, V-M., Viisanen, Y., Hari,
2 P., Bondur, V., Kasimov, N., Kotlyakov, V., Matvienko, G., Baklanov, A., Guo, H., Ding, A.,
3 Hansson, H-C., and Zilitinkevich, S., 2015. Introduction: The Pan-Eurasian Experiment (PEEX)
4 – multi-disciplinary, multi-scale and multi-component researchn and capacity building
5 initiative, *Atmos. Chem. Phys.*, 15, 13085-13096, doi:10.5194/acp-15-13085-2015, 2015.

6 Langenfelds, R. L., Francey, R. J., Pak, B. C., Steele, L. P., Lloyd, J., Trudinger, C. M., and
7 Allison, C. E.: Interannual growth rate variations of atmospheric CO₂ and its delta C-13, H-2,
8 CH₄, and CO between 1992 and 1999 linked to biomass burning, *Global Biogeochem. Cy.*, 16,
9 Artn 1048, doi:10.1029/2001gb001466, 2002.

10 Lappalainen, H.K. et al., Pan-Eurasian Experiment (PEEX): Towards holistic understanding of
11 the feedbacks and interactions in the land-atmosphere-ocean-society continuum in the Northern
12 Eurasian region, submitted to *Atmos. Chem. Phys.*, 2016.

13 Lau, K. M., Kim, M. K., and Kim, K. M.: Asian summer monsoon anomalies induced by aerosol
14 direct forcing: the role of the Tibetan Plateau, *Clim. Dynam.*, 26, 855-864, doi:10.1007/s00382-
15 006-0114-z, 2006.

16 Li, J. F., Song, Y., Mao, Y., Mao, Z. C., Wu, Y. S., Li, M. M., Huang, X., He, Q. C., and Hu,
17 M.: Chemical characteristics and source apportionment of PM_{2.5} during the harvest season in
18 eastern China's agricultural regions, *Atmos. Environ.*, 92, 442-448, 10.1016/j.atmosenv.
19 2014.04.058, 2014.

20 Li, M., Zhang, Q., Kurokawa, J., Woo, J., He, K., Lu, Z., Ohara, T., Song, Y., Sreets, D., and
21 Carmichael, G.: MIX: a mosaic Asian anthropogenic emission inventory for the MICS-Asia
22 and the HTAP projects, *Atmos. Phys. Chem. Discuss.*, 34813-34869, doi:10.5194/acpd-15-
23 34813-2015, 2015.

24 Lin, Y. L., Farley, R. D., and Orville, H. D.: Bulk Parameterization of the Snow Field in a Cloud
25 Model, *J. Clim. Appl. Meteorol.*, 22, 1065-1092, doi: 10.1175/1520-0450(1983)022<1065:
26 Bpotsf>2.0.Co;2, 1983.

27 Liu, Y., Fu, R., and Dickinson, R.: Smoke aerosols altering South American monsoon, *B. Am.*
28 *Meteorol. Soc.*, 86, 1062-1063, 2005.

29 Lo, J. C. F., Yang, Z. L., and Pielke, R. A.: Assessment of three dynamical climate downscaling
30 methods using the Weather Research and Forecasting (WRF) model, *J. Geophys. Res. Atmos.*,
31 113, Artn D09112, doi:10.1029/2007jd009216, 2008.

32 Menon, S., Hansen, J., Nazarenko, L., and Luo, Y. F.: Climate effects of black carbon aerosols
33 in China and India, *Science*, 297, 2250-2253, doi:10.1126/science.1075159, 2002.

34 Mlawer, E. J., Taubman, S. J., Brown, P. D., Iacono, M. J., and Clough, S. A.: Radiative transfer
35 for inhomogeneous atmospheres: RRTM, a validated correlated-k model for the longwave, *J.*
36 *Geophys. Res. Atmos.*, 102, 16663-16682, doi:10.1029/97jd00237, 1997.

37 NBSC: China Statistical Yearbook National Bureau of Statistics of China ed., China Statistics
38 Press, Beijing, 2013.

39 Penner, J. E., Dickinson, R. E., and Oneill, C. A.: Effects of Aerosol from Biomass Burning on
40 the Global Radiation Budget, *Science*, 256, 1432-1434, doi:10.1126/science.256. 5062.1432,
41 1992.

42 Procopio, A. S., Artaxo, P., Kaufman, Y. J., Remer, L. A., Schafer, J. S., and Holben, B. N.:
43 Multiyear analysis of amazonian biomass burning smoke radiative forcing of climate, *Geophys.*
44 *Res. Lett.*, 31, Artn L03108, doi:10.1029/2003gl018646, 2004.

1 Ramanathan, V., Chung, C., Kim, D., Bettge, T., Buja, L., Kiehl, J. T., Washington, W. M., Fu,
2 Q., Sikka, D. R., and Wild, M.: Atmospheric brown clouds: Impacts on South Asian climate
3 and hydrological cycle, *P. Natl. Acad. Sci. USA*, 102, 5326-5333, 10.1073/pnas.0500656102,
4 2005.

5 Ramanathan, V., and Carmichael, G.: Global and regional climate changes due to black carbon,
6 *Nat Geosci*, 1, 221-227, 10.1038/ngeo156, 2008.

7 Reid, J. S., Hobbs, P. V., Lioussse, C., Martins, J. V., Weiss, R. E., and Eck, T. F.: Comparisons
8 of techniques for measuring shortwave absorption and black carbon content of aerosols from
9 biomass burning in Brazil, *J. Geophys. Res. Atmos.*, 103, 32031-32040, doi:10.
10 1029/98jd00773, 1998.

11 Reid, J. S., Koppmann, R., Eck, T. F., and Eleuterio, D. P.: A review of biomass burning
12 emissions part II: intensive physical properties of biomass burning particles, *Atmos. Chem.*
13 *Phys.*, 5, 799-825, 2005.

14 Robock, A.: Enhancement of Surface Cooling Due to Forest Fire Smoke, *Science*, 242, 911-
15 913, 1988.

16 Robock, A.: Surface Cooling Due to Forest-Fire Smoke, *J. Geophys. Res. Atmos.*, 96, 20869-
17 20878, doi:10.1029/91jd02043, 1991.

18 Rosenfeld, D.: TRMM observed first direct evidence of smoke from forest fires inhibiting
19 rainfall, *Geophys. Res. Lett.*, 26, 3105-3108, doi:10.1029/1999gl006066, 1999.

20 Rosenfeld, D., Lohmann, U., Raga, G. B., O'Dowd, C. D., Kulmala, M., Fuzzi, S., Reissell, A.,
21 and Andreae, M. O.: Flood or drought: How do aerosols affect precipitation?, *Science*, 321,
22 1309-1313, 10.1126/science.1160606, 2008.

23 Roy, D. P., and Boschetti, L.: Southern Africa Validation of the MODIS, L3JRC, and
24 GlobCarbon Burned-Area Products, *IEEE T. Geosci. Remote*, 47, 1032-1044,
25 10.1109/Tgrs.2008.2009000, 2009.

26 Ryu, S. Y., Kwon, B. G., Kim, Y. J., Kim, H. H., and Chun, K. J.: Characteristics of biomass
27 burning aerosol and its impact on regional air quality in the summer of 2003 at Gwangju, Korea,
28 *Atmos. Res.*, 84, 362-373, 10.1016/j.atmosres.2006.09.007, 2007.

29 Sakaeda, N., Wood, R., and Rasch, P. J.: Direct and semidirect aerosol effects of southern
30 African biomass burning aerosol, *J. Geophys. Res. Atmos.*, 116, Artn D12205, doi:
31 10.1029/2010jd015540, 2011.

32 Saleh, R., Robinson, E. S., Tkacik, D. S., Ahern, A. T., Liu, S., Aiken, A. C., Sullivan, R. C.,
33 Presto, A. A., Dubey, M. K., Yokelson, R. J., Donahue, N. M., and Robinson, A. L.: Brownness
34 of organics in aerosols from biomass burning linked to their black carbon content, *Nat. Geosci.*,
35 7, 647-650, 10.1038/NCEO2220, 2014.

36 Schwarz, J. P., Gao, R. S., Spackman, J. R., Watts, L. A., Thomson, D. S., Fahey, D. W.,
37 Ryerson, T. B., Peischl, J., Holloway, J. S., Trainer, M., Frost, G. J., Baynard, T., Lack, D. A.,
38 de Gouw, J. A., Warneke, C., and Del Negro, L. A.: Measurement of the mixing state, mass,
39 and optical size of individual black carbon particles in urban and biomass burning emissions,
40 *Geophys. Res. Lett.*, 35, Artn L13810, doi:10.1029/2008gl033968, 2008.

41 Simpson, J., Adler, R. F., and North, G. R.: A Proposed Tropical Rainfall Measuring Mission
42 (Trmm) Satellite, *B. Am. Meteorol. Soc.*, 69, 278-295, doi:10.1175/1520-0477(1988)069
43 <0278:Aptrmm>2.0.Co;2, 1988.

1 Tao, W. K., J. P. Chen, Z. Q. Li, C. Wang, and C. D. Zhang, Impact of Aerosols on
2 Convective Clouds and Precipitation, *Reviews of Geophysics*, 50, doi:10.1029/2011rg000369,
3 2012.

4 van der Werf, G. R., Randerson, J. T., Giglio, L., Collatz, G. J., Kasibhatla, P. S., and Arellano,
5 A. F.: Interannual variability in global biomass burning emissions from 1997 to 2004, *Atmos.*
6 *Chem. Phys.*, 6, 3423-3441, 2006.

7 Wang, M., S. Ghan, M. Ovchinnikov, X. Liu, R. Easter, E. Kassianov, Y. Qian, and H. Morrison,
8 Aerosol indirect effects in a multi-scale aerosol-climate model PNNL-MMF, *Atmos. Chem.*
9 *Phys.*, 11(11), 5431-5455, doi:10.5194/Acp-11-5431-2011, 2011.

10 Wiedinmyer, C., Quayle, B., Geron, C., Belote, A., McKenzie, D., Zhang, X. Y., O'Neill, S.,
11 and Wynne, K. K.: Estimating emissions from fires in North America for air quality modeling,
12 *Atmos. Environ.*, 40, 3419-3432, 10.1016/j.atmosenv.2006.02.010, 2006.

13 Wiedinmyer, C., Akagi, S. K., Yokelson, R. J., Emmons, L. K., Al-Saadi, J. A., Orlando, J. J.,
14 and Soja, A. J.: The Fire INventory from NCAR (FINN): a high resolution global model to
15 estimate the emissions from open burning, *Geosci. Model Dev.*, 4, 625-641, doi:10.5194/gmd-
16 4-625-2011, 2011.

17 Xie, Y. N., Ding, A. J., Nie, W., Mao, H. T., Qi, X. M., Huang, X., Xu, Z., Kerminen, V. M.,
18 Petaja, T., Chi, X. G., Virkkula, A., Boy, M., Xue, L. K., Guo, J., Sun, J. N., Yang, X. Q.,
19 Kulmala, M., and Fu, C. B.: Enhanced sulfate formation by nitrogen dioxide: Implications from
20 in situ observations at the SORPES station, *J. Geophys. Res. Atmos.*, 120, 12679-12694,
21 10.1002/2015JD023607, 2015.

22 Yan, X. Y., Ohara, T., and Akimoto, H.: Bottom-up estimate of biomass burning in mainland
23 China, *Atmos. Environ.*, 40, 5262-5273, 10.1016/j.atmosenv.2006.04.040, 2006.

24 Yang, S. J., He, H. P., Lu, S. L., Chen, D., and Zhu, J. X.: Quantification of crop residue burning
25 in the field and its influence on ambient air quality in Suqian, China, *Atmos. Environ.*, 42, 1961-
26 1969, 10.1016/j.atmosenv.2007.12.007, 2008.

27 Zaveri, R. A., and Peters, L. K.: A new lumped structure photochemical mechanism for large-
28 scale applications, *J. Geophys. Res. Atmos.*, 104, 30387-30415, 1999.

29 Zaveri, R. A., Easter, R. C., Fast, J. D., and Peters, L. K.: Model for simulating aerosol
30 interactions and chemistry (MOSAIC), *J. Geophys. Res. Atmos.*, 113, D13204, 2008.

31 Zhang, Y., Fu, R., Yu, H., Qian, Y., Dickinson, R., Silva Dias, M. A. F., da Silva Dias, P. L.,
32 and Fernandes, K.: Impact of biomass burning aerosol on the monsoon circulation transition
33 over Amazonia, *Geophys. Res. Lett.*, 36, 2009.

34 Zhao, C., Leung, L. R., Easter, R., Hand, J., and Avise, J.: Characterization of speciated aerosol
35 direct radiative forcing over California, *J. Geophys. Res. Atmos.*, 118, 2372-2388,
36 10.1029/2012JD018364, 2013.

37 Zhao, T., and Yatagai, A.: Evaluation of TRMM 3B42 product using a new gauge - based
38 analysis of daily precipitation over China, *Int. J. Climatol.* 34, 2749-2762, 2014.

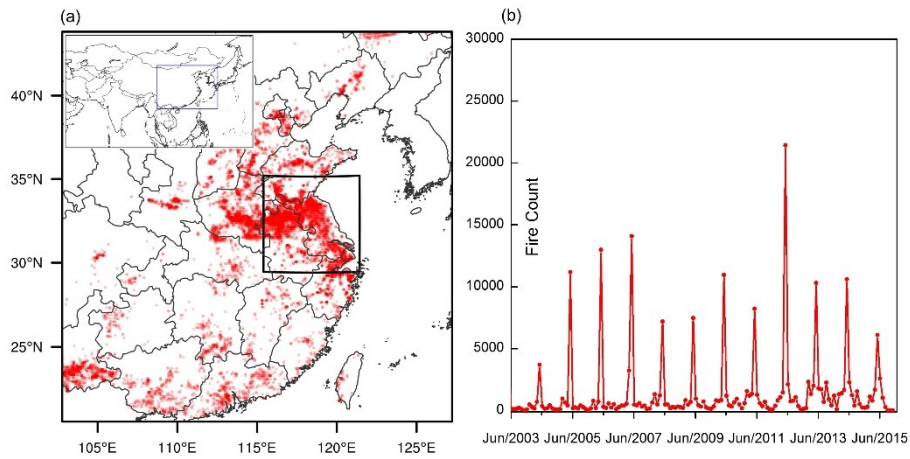


Figure 1. (a) Distribution of 13-year total fire detections by MOD14A1 during 2003–2015 in the WRF-Chem coarse domain. The black rectangle represents the inner domain. The top left corner gives a map showing the geographic location of the model domain. (b) 13-year time series of monthly fire detections in the model coarse domain based on MOD14A1 retrievals.

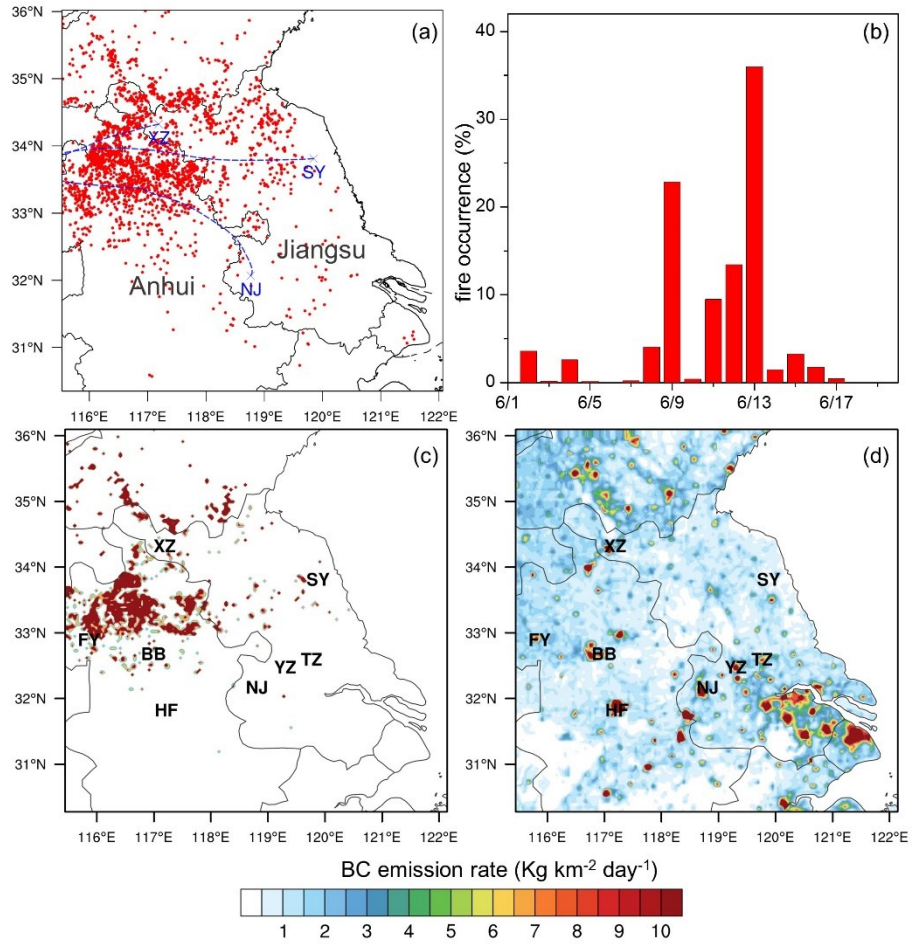


Figure 2. (a) Satellite fire detections in June 2012 and backward trajectories for NJ (Nanjing), XZ (Xuzhou) and SY (Sheyang), (b) Temporal variations of daily fire occurrences. BC emission rates from (c) agricultural fires and (d) anthropogenic activities on 9 June. Note that the backward trajectories was calculated for an altitude of 2 km over NJ, XZ, and SY from 14:00 LT, 18:00 LT on 10 June and 01:00 on 11 June. Anhui and Jiangsu province are labelled in gray in Fig. 2a.

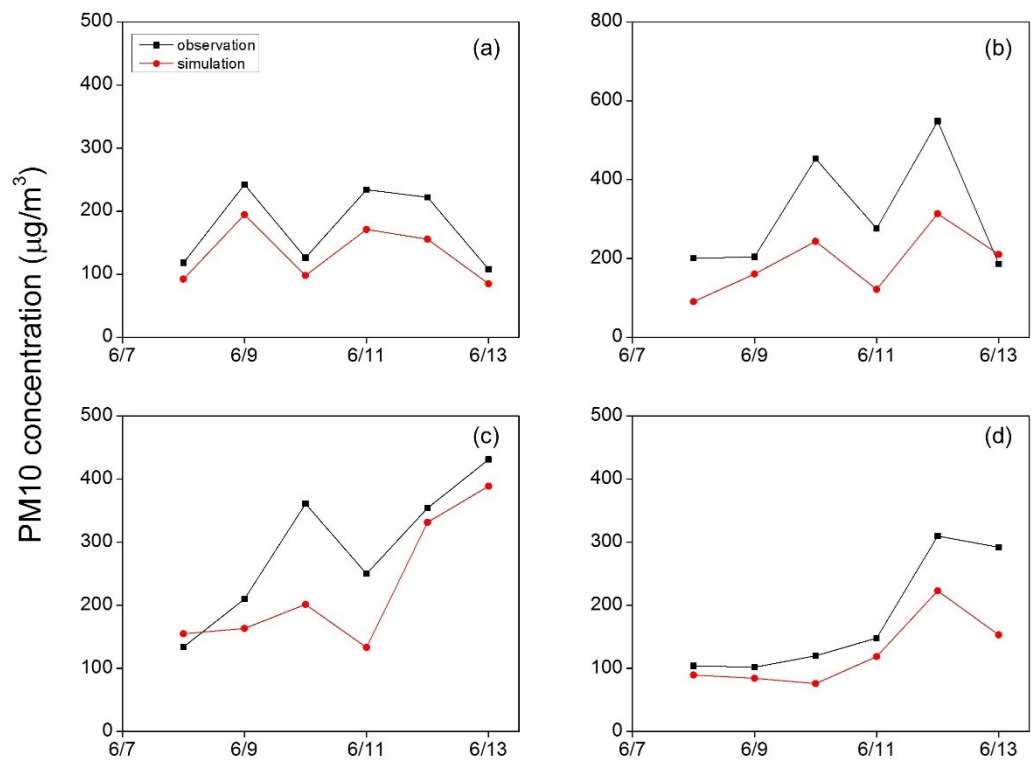


Figure 3. Measurements of 24-hour averaged PM₁₀ concentrations and corresponding PM₁₀ simulations at (a) FY (Fuyang), (b) BB (Bengbu), (c) XZ (Xuzhou) and (d) HF (Hefei).

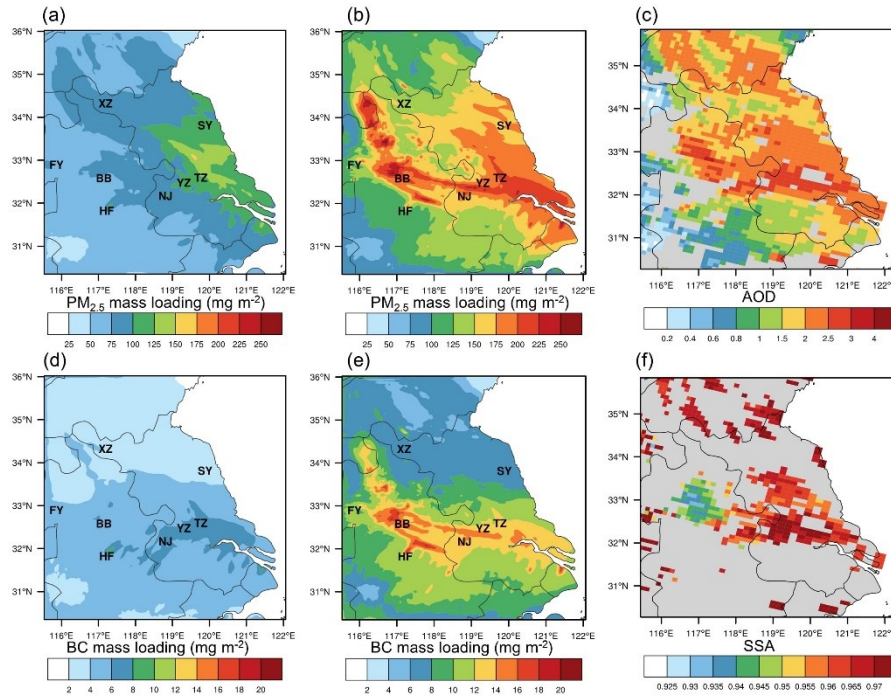


Figure 4. Spatial distributions of simulated PM_{2.5} mass loading by (a) ARI-A and (b)ARI-AB experiment, and (c) satellite-derived 660-nm AOD at 11:00 LT, 9 June. Simulated BC mass loading by (d) ARI-Aand (e) ARI-AB experiment and (f) satellite-derived SSA at that time.

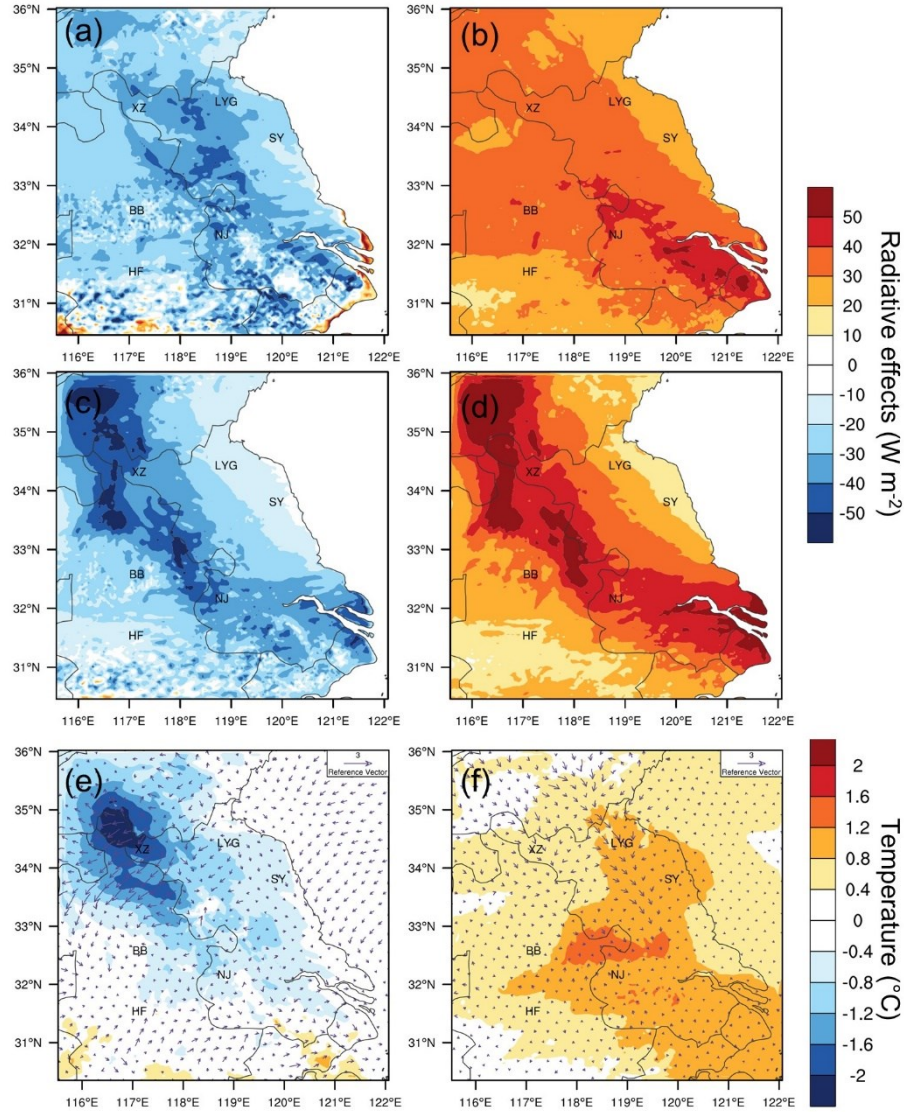


Figure 5. Radiative forcing (a) at the surface and (b) in the atmosphere due to anthropogenic aerosols on 10 June. Radiative forcing of aerosol (c) at the surface and (d) in the atmosphere due to biomass burning emissions on 10 June. Aerosol-induced changes in air temperature and wind fields (e) near the surface and (f) at the altitude of 2 km.

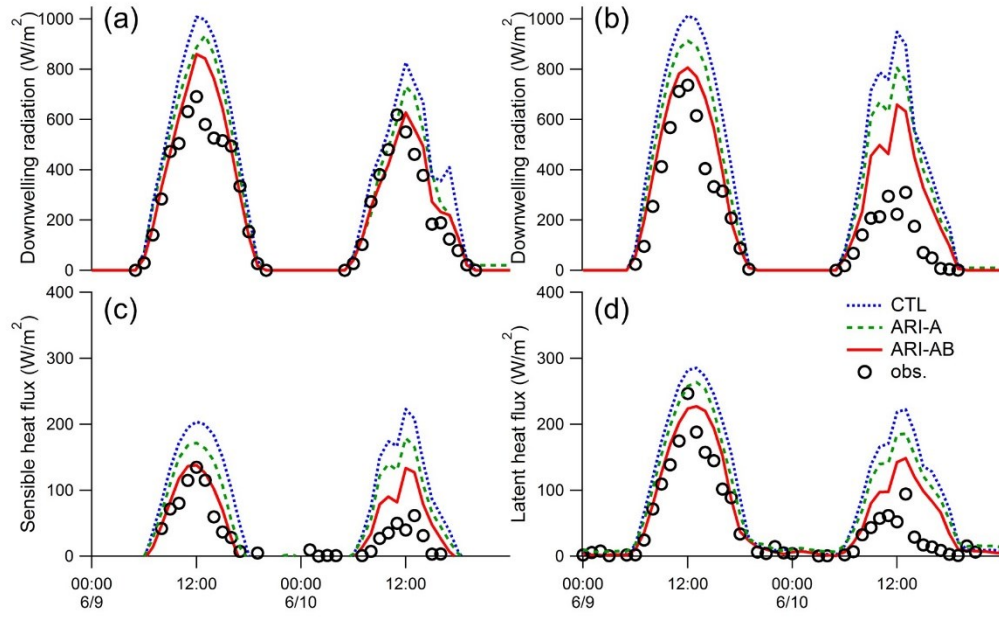


Figure 6. Diurnal variations of simulated and observed downwelling short-wave radiation at (a) HF (Hefei) and (b) NJ (Nanjing) on 9-10, June. Comparisons of simulated sensible (c) and latent heat fluxes (d) with the measurements at NJ. Blue, green and red lines present CTL, ARI-A and ARI-AB experiments. Black circles mark the observations.

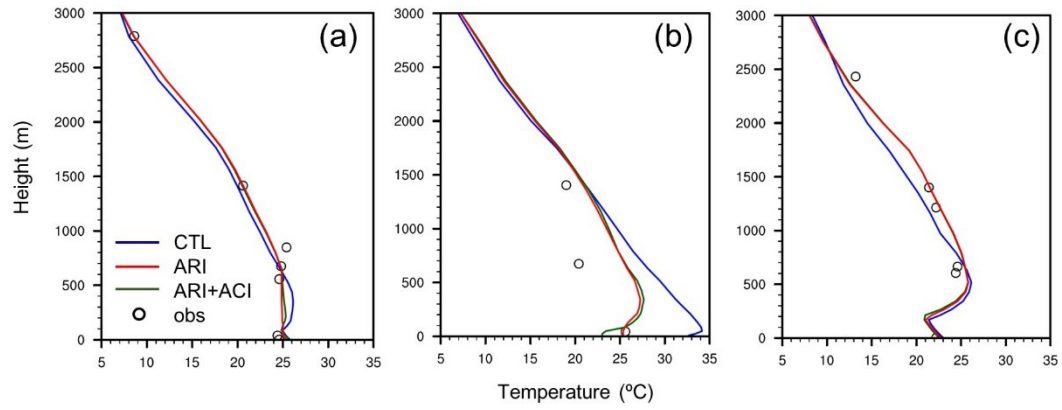


Figure 7. Comparisons between the observed and modelled air temperature profiles for (a) NJ (Nanjing) at 08:00LT, (b) XZ (Xuzhou) and (c) SY (Sheyang) at 20:00 LT, 10 June. Black circles denote sounding observations. Blue, green and red solid lines are experiments without (CTL) and with radiative effects of aerosols from anthropogenic emissions (ARI-A) and additional fire emissions (ARI-AB), respectively.

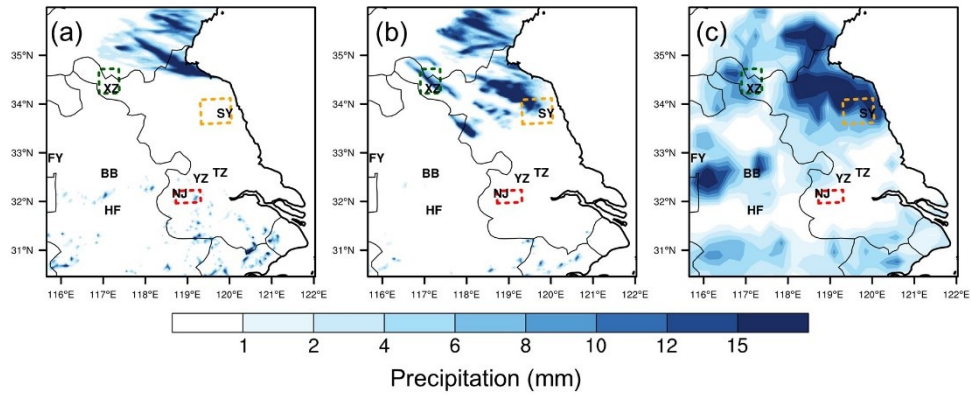


Figure 8. Modelled precipitation during the period from 00:00 UTC, 10 June to 00:00 UTC, 11 June while excluding and considering radiative effects of aerosols in (a) CTL and (b) ARI-AB experiment, corresponding with (c) TRMM-observed precipitation. Three regions with notable changes in precipitation are marked in rectangles: Zone 1 (red dashed line), Zone 2 (green dashed line) and Zone 3 (yellow dashed line).

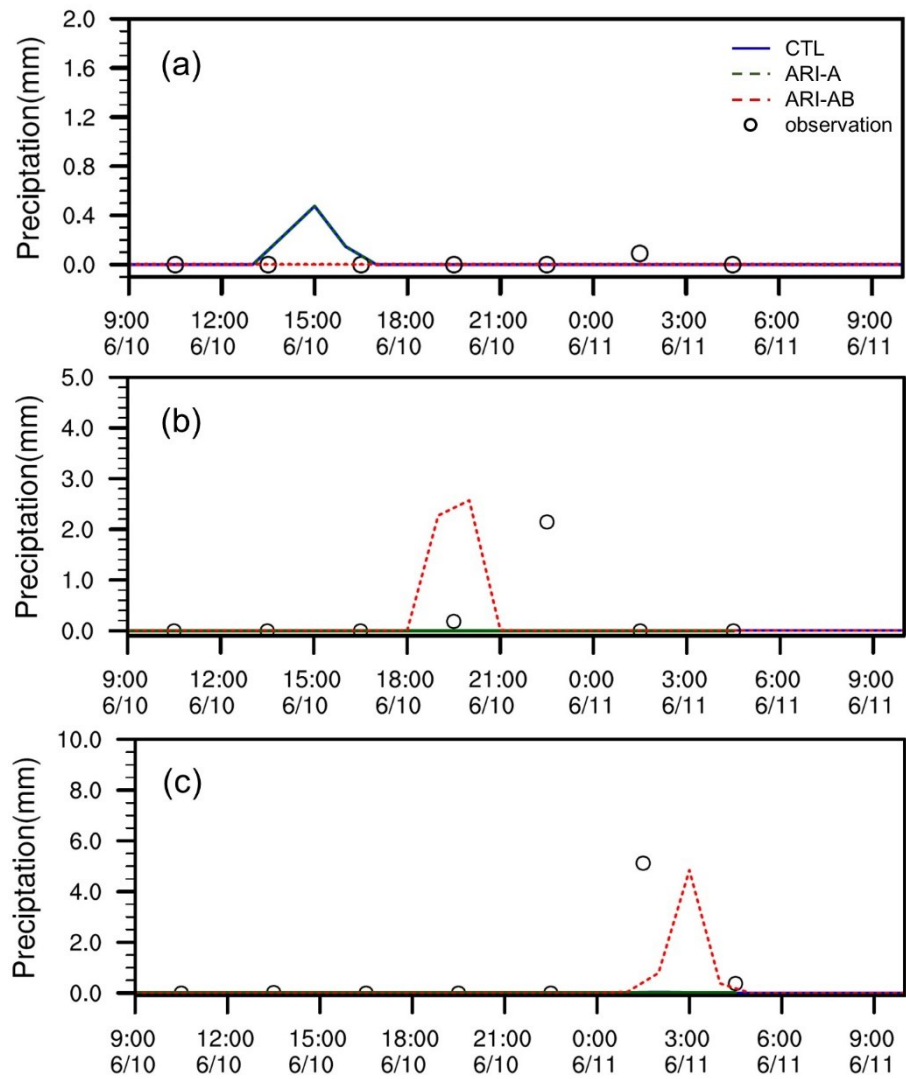


Figure 9. Simulated hourly precipitation while considering (ARI-A experiment in green dashed lines; ARI-AB experiment in red dashed lines) and excluding (blue solid lines, CTL) radiative effects of aerosols, and their comparisons with TRMM observations (black circles) for (a) Zone1, (b) Zone 2 and (c) Zone 3.

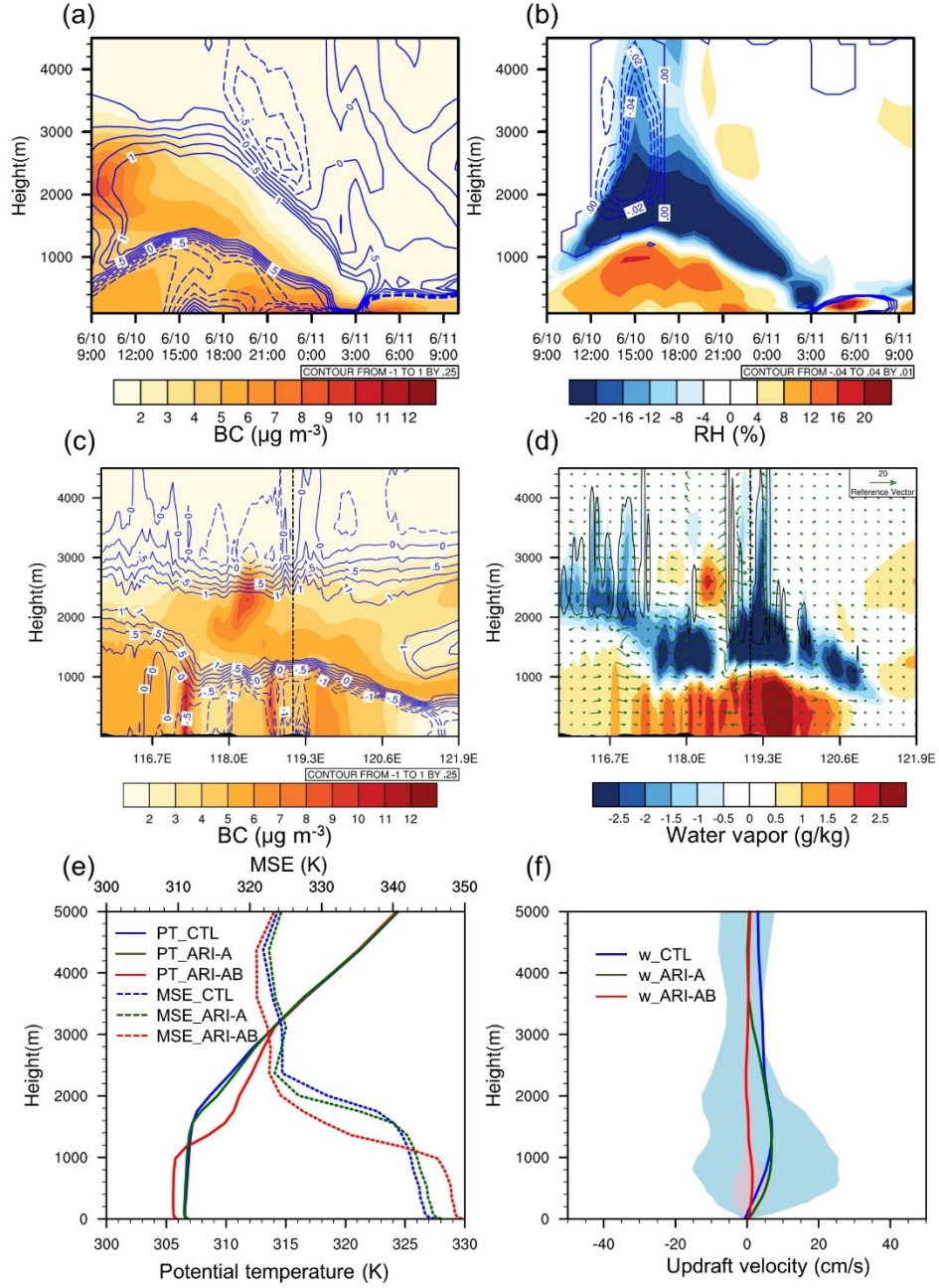


Figure 10. (a) Temporal evolutions of BC vertical profile and changes in air temperature (K), (b) perturbations in RH (%) and cloud water (g kg^{-1}) over Zone 1. (c) Longitude-height cross sections of BC concentrations and aerosol-induced temperature changes at 14:00 LT, 10 June. (d) same as (c) but for water vapor (g kg^{-1}) and wind fields (m s^{-1}). Note that the vertical wind speed was multiplied by a factor of 100. Red and black lines in (d) outline cloud coverage (cloud water mass ratio greater than $10^{-3} \text{ g kg}^{-1}$) in ARI-AB and CTL simulation. In this case, the condensate mass ratio was less than $10^{-3} \text{ g kg}^{-1}$ for the whole column in ARI-AB, thus no red line is presented in Fig.10d. (e) Vertical profile of zone-averaged potential temperature (PT) and MSE, and (f) updraft velocity predicted by CTL (blue), ARI-A (green) and ARI-AB (red) at 14:00 LT. Shadows in Fig.10f represent 25-75 percentile range of simulated updraft velocity.

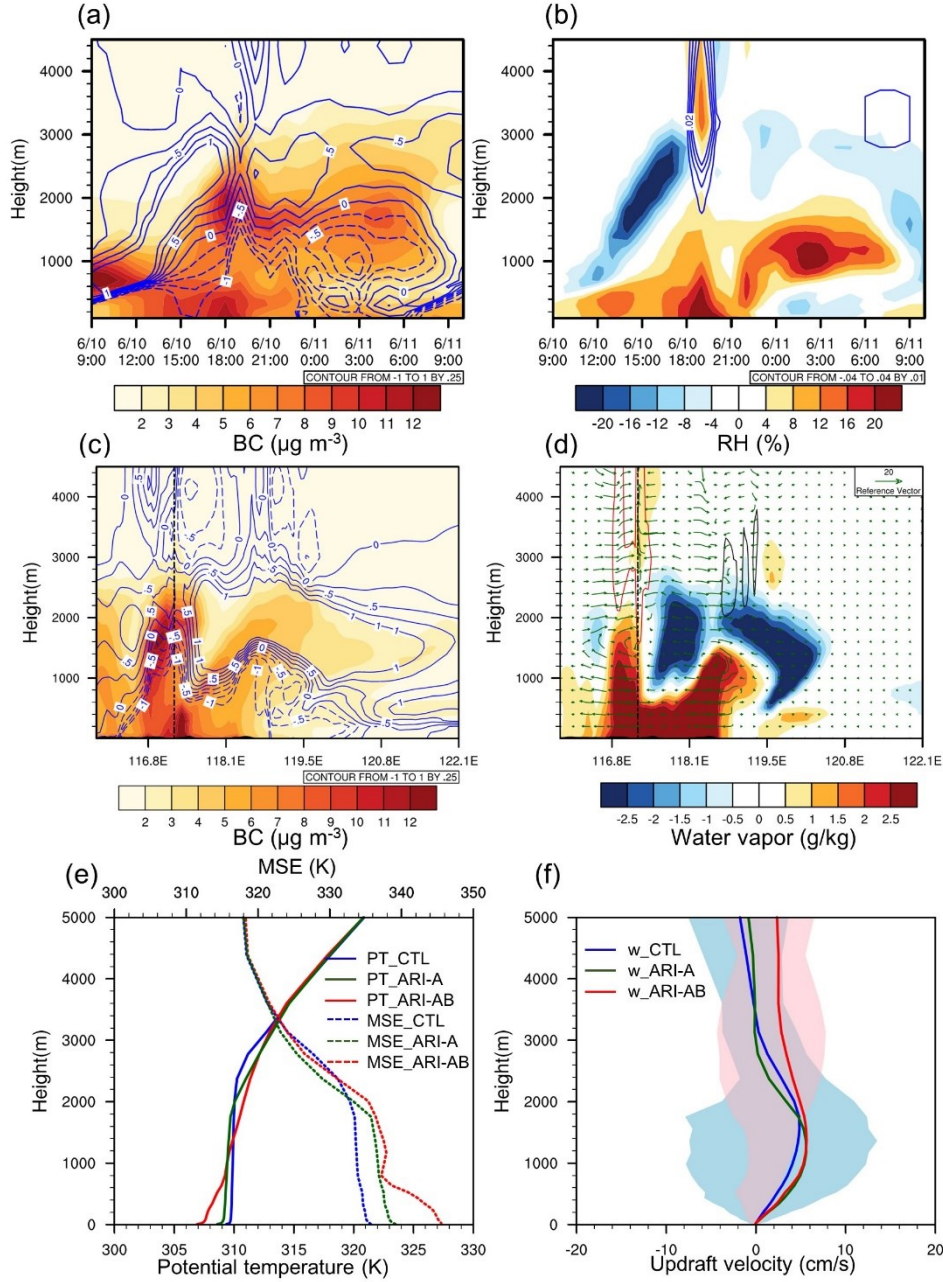


Figure 11. (a) Temporal evolutions of BC vertical profile and changes in air temperature (K), (b) perturbations in RH (%) and cloud water (g kg^{-1}) over Zone 2. (c) Longitude-height cross sections of BC concentrations and aerosol-induced temperature changes at 18:00 LT, 10 June. (d) same as (c) but for water vapor (g kg^{-1}) and wind fields (m s^{-1}). Note that the vertical wind speed was multiplied by a factor of 100. Red and black lines in (d) outline cloud coverage (cloud water mass ratio greater than $10^{-3} \text{ g kg}^{-1}$) in ARI-AB and CTL simulation. (e) Vertical profile of zone-averaged potential temperature (PT) and MSE, and (f) updraft velocity predicted by CTL (blue), ARI-A (green) and ARI-AB (red) at 18:00 LT. Shadows in f represent 25-75 percentile range of simulated updraft velocity.

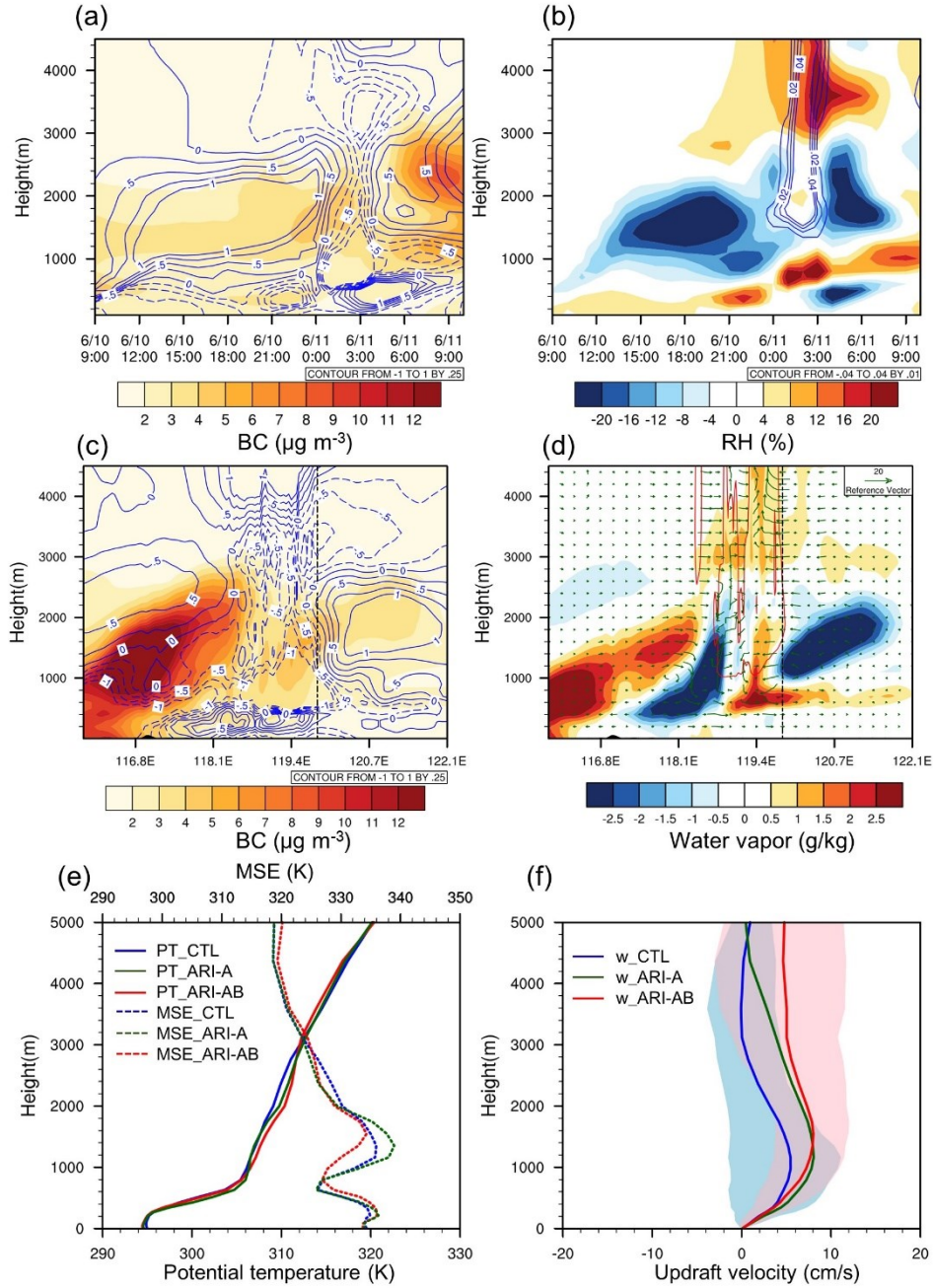


Figure 12. (a) Temporal evolutions of BC vertical profile and changes in air temperature (K), (b) perturbations in RH (%) and cloud water (g kg⁻¹) over Zone 3. (c) Longitude-height cross sections of BC concentrations and aerosol-induced temperature changes at 01:00 LT, 11 June. (d) same as (c) but for water vapor (g kg⁻¹) and wind fields (m s⁻¹). Note that the vertical wind speed was multiplied by a factor of 100. Red and black lines in (d) outline cloud coverage (cloud water mass ratio greater than 10⁻³ g kg⁻¹) in ARI-AB and CTL simulation. In this case, the condensate mass ratio was less than 10⁻³ g kg⁻¹ for the whole column in CTL, thus no black line is presented in Fig.12d. (e) Vertical profile of zone-averaged potential temperature (PT) and MSE, and (f) updraft velocity predicted by CTL (blue), ARI-A (green) and ARI-AB (red) at 01:00 LT. Shadows in Fig.12f represent 25-75 percentile range of simulated updraft velocity.